DESIGN SIMULATION AND CONSTRUCTION OF PARTICLE AND ACCELERATOR DETECTORS

by

Ezgi Ergenlik

B.S., Physics, Boğaziçi University, 2015

Submitted to the Institute for Graduate Studies in
Science and Engineering in partial fulfillment of
the requirements for the degree of
Master of Science

Graduate Program in Physics

Boğaziçi University

2018

ACKNOWLEDGEMENTS

This thesis become reality with the help and support of many people and I would like to thank all of them.

As a beginning I would like to start with two people, Erkcan Özcan and Gökhan Ünel who have always been there for me. It is a genuine pleasure to express my thanks and gratitude to Erkcan Özcan who has always supported me and restored my curiosity and deep belief in science with his belief in all of human kind and his beautiful mind. Also I owe a deep sense of gratitude to Gökhan Ünel who has always challenged me to uncover the best in me with his passion for science and his endless determination for work. They have separately done a lot of things for this thesis and my knowledge about physics, but they also together made me who I am now and I will always be glad to have both of them in my life which makes me the luckiest person in the world.

I would like to thank BOUN KAHVE Lab team who has always supported me and lent their assistance when I needed their support.

I would like to thank Aytül Adıgüzel and Saime Gürbüz for their support and help in the BOUN GETO project and also for their contribution to my learning process.

I would like to thank Alperen Yüncü and Salim Oğur who have always assisted me in my academic life but also they are really good friends who have listened to me and have given me the most important advices when i needed them.

Finally, I would like to thank my parents, Ümmühan and Yılmaz Ergenlik, who have always been there for me, supported me and kept my happiness above everything. They gave me the courage to to do everything that I truly want. Their love and support are the most important things in the world.

ABSTRACT

DESIGN SIMULATION AND CONSTRUCTION OF PARTICLE AND ACCELERATOR DETECTORS

As a part of the research being carried out at Bogazici University, Kandilli Detector, Accelerator And Instrumentation Laboratory, there was a need for beam-parameter-measurement devices and tools such AC current transformer for particle beam current measurements and Delay Wire Chamber (DWC) for particle beam profile measurements etc. In order to satisfy this need and the similar ones that will potentially arise due to the anticipated construction of particle accelerators in Turkey, a multi-pronged study has been conducted. First, an AC current transformer was designed, produced and tested on a proton beam line to measure the beam current. Second, in order to measure the beam profile, a suitable delay-wire-chamber was designed, produced and tested using cosmic rays; and finally a beam transport program was written to observe the changes on the beam parameters of a generic beam line. In this thesis, these aforementioned efforts are presented and the results are discussed.

ÖZET

PARÇACIK VE HIZLANDIRICI DEDEKTÖRLERİNİN TASARIMI,BENZETİMİ VE ÜRETİMİ

Boğaziçi Üniversitesi Kandilli Algıç, Hızlandırıcı Ve Enstürmantasyon(KAHVE) Laboratuvarı'nda yapılan çalışmalar için parçacık hızlandırıcılarında demet parametrelerinin ölçümlerine yönelik (demet akımının ölçümü için kullanılacak bir AC akım transformatörü ya da demet profili ölçümü için kullanılacak bir Gecikmeli tel odası (GETO) gibi cihaz ve yöntemlere ihtiyaç duyulmaktadır. Hem bu ihtiyaç, hem de ülkemizde inşa edilmesi öngörülen çeşitli parçacık hızlandırıcılarının gereksinimleri göz önünde bulundurularak, çok yönlü bir çalışma gerçekleştirilmiştir. Öncelikle parçacık demetinin akımının ölçülmesi için bir AC akım trafosu tasarlanmış, üretilmiş ve bir demet hattında denenmiş, sonra demet profilinin belirlenebilmesine uygun özelliklerde bir gecikmeli tel odası tasarlanmış, üretilmiş ve kozmik ışın sinyallerini alabildiği görülüp son olarak da demet parametrelerinin hat boyunca değişiminin belirlenebileceği bir demet taşıma programı yazılmıştır. Bu çalışmalar özetlenecek ve ulaşılan sonuçlar tartışılacaktır.

TABLE OF CONTENTS

LIST OF FIGURES

LIST OF TABLES

LIST OF SYMBOLS

B	Magnetic Field
C	Capacitance
E	Electric field
f	Frequency
g	Quadrupole magnet gradient
i_s	Induced current
i_b	beam current
k	Quadrupole strength
L	inductance
M	Multiplication factor
n_s	Number of turns in the winding
P	Momentum
s	trajectory of synchronus particle
T	Transfer Matrix
$\mathbf{w}$	Drift velocity
W_I	Average energy per ion pair
α	Twiss parameter alpha
β	Twiss parameter beta
γ	Twiss parameter gamma
γ_{rel}	relativistic gamma
β_{rel}	relativistic particle velocity
ε	emittance
λ	Mean free path
μ	Mobility
ρ	Bending radius
σ_{ij}	The elements of the beam matrix

LIST OF ACRONYMS/ABBREVIATIONS

AC	Alternating current
CERN	Conseil Européen pour la Recherche Nucléaire
DC	Direct current
DWC	Delay Wire Chamber
FR4	Flame Retardant 4
LEBT	Low Energy Beam Transport
MWPC	Multi wire proportional chamber
OPAMP	Operational Amplifier
PCB	Printed Circuit Board
PMT	Photo Multiplier Tube
RFQ	Radio Frequency Quadrupole
SANAEM	Sarayköy Nükleer Araştırma Merkezi
SPICE	Simulation Program with Integrated Circuit Emphasis
SPS	Super Proton Synchrotron

1. INTRODUCTION

Efforts based on the understanding of the world began to be perceived by the human eye, and later it became increasingly curious to the micro or macro world. For example, telescopes were used to observe very large objects and later starting from magnifiers to microscopes a lot of tools were invented for microscopic objects. When it came to investigate smaller particles that could not even be seen with electron microscopes, a new method was needed. Particle detectors and accelerators have emerged as a result of this need. Today, they do not only help to understand the micro world, but also their usage in many other areas in daily life are increasing day by day. A particle detector is a device that measures the energy, momentum, position, spin etc. of the particles. Although there are many types of particle detectors such as calorimeters, solid state detectors etc., in this work It will be also focusing on the gaseous detectors and AC current transformers which are both used in accelerator physics.

Particle detectors play important roles in the defense industry, imaging technology and medicine, Although the most basic field of use is scientific experiments. In addition to being used for identification of subatomic particles, particle detectors are also used for beam diagnostics. Beam diagnostics involve measurements of many properties of a beam, such as its emittance, size, current and profile. Particle detectors are generally used for measuring the charged particles or charged beams. Charged beams creates ionization inside a gas which allows us to identify the specifications of the beams. Furthermore, they are ideal current sources which means we can have informations about the beam properties if the electric and magnetic fields created by the charged particles are measured.

The AC Current Transformer is a type of sensor that produces an alternating current in its secondary winding proportional to the current in the primary section. The working principle depends on the basic law which is the varying magnetic field induces current. Due to the operational logic of the transformers, the incoming signal is small and it needs an amplification circuit to measure the current.

Working principle of gaseous detectors depends on the ionization of gas molecules by the incoming particle, with resulting electrons and ions generating signal to be measured. Broadly speaking, there are three types of gaseous detectors which are ionization chambers, proportional counters, Geiger-Müller tubes. Proportional chambers like Multi Wire Proportional Chamber(MWPC) and Delay Wire Chambers(DWC) are still used in the extraction sections of the beam lines such as SPS. Especially MWPC and DWC have been used many years in the proton-anti proton and heavy ion extraction lines at CERN .

Particle detectors and accelerators are not cheap and easy-to-construct devices therefore detailed calculations and simulations before their production are crucial for researchers. The calculations can be time consuming as extensive numerical analyses need to be performed. We propose that some of the detector components can be designed with the freely available tools and can be constructed using raw materials and know-how from the local manufacturers. That is why this work also contains results from the existing programs, new simulation program for beam diagnostic and a comparison measurement from actual devices.

2. ACCT: BEAM CURRENT AND ENERGY MEASUREMENTS

AC Current transformer (ACCT) is a device which can be used to measure the current of the beam. The energy measurement also can be performed using two ACCTs to determine the time of flight of the beam between two stations, which can be converted to velocity. The advantage of the ACCT is that it does not disturbed the beam, i.e. no particle loss or change in the beam. This part of the thesis only contains the current measurements of SANAEM Project Prometheus (SPP) beam line with ACCT because technical problems in the beam line did not allow us to measure the energy of the particles.

2.1. Theory

Inductors create voltage signal proportional to change in magnetic field which can be used to measure beam current. In Figure 2.1, a pulsed beam is taken as the primary current source which creates varying magnetic field in its vicinity as forseen by Maxwell's equations, which in turn generates a current in the secondary winding. Current in the secondary winding is generally quite small so an amplifying circuit is needed.

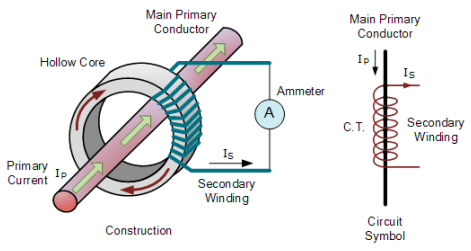

Figure 2.1. ACCT working principle scheme [4]

From Faraday's Law, the induced potential V is :

$$V = n_s \frac{d\Phi_s}{dt} = Ri_s \tag{2.1}$$

$$V = L\frac{di_b}{dt} \tag{2.2}$$

$$\int V dt = \int L di_b \tag{2.3}$$

Where n_s is the number of turns in the winding, Φ_s is the total flux in the magnetic core , i_s is the induced current on the second winding, i_b is the beam current and L is the inductance of the coil. Inductance is an important parameter which depends on the magnetic core. As can be seen in the formula, higher inductance causes higher voltage, which leads us to choose high inductance material.

There are three types of current transformers: wound, toroidal and bar. In this work, toroidal current transformers have been used. The toroidal current transformer does not have a primary winding, instead beam performs the same task.

For finding the beam current, the integral in Equation 2.3 should be taken. Instead of taking this integral by hand, an electronic circuit can be constructed to perform the operation automatically. An inverting integrating amplifying circuit was constructed with an operational amplifier, resistances and capacitors. It should also be a low pass filter to eliminate high frequency noise.

Simple inverting amplifiers with no integrator consist of an opamp and two resistors. Basic implementation can be seen in Figure 2.2. Its gain is easy to compute taking the underground input of the opamp as vitual ground and using Kirchhoff's law at that point:

$$Gain = \frac{V_{out}}{V_{in}} = -\frac{R_f}{R_{in}} \tag{2.4}$$

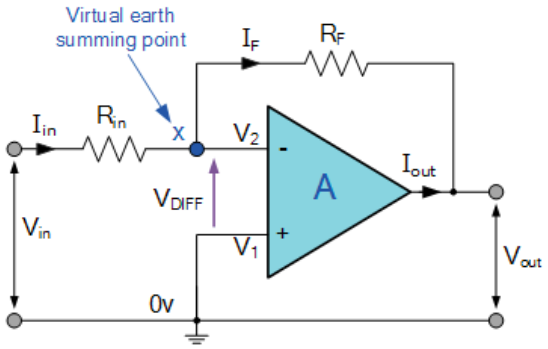

Figure 2.2. Inverting operational opamp circuit [4]

ACCT requires an integrator so a capacitor connected in parallel to the R_f resistor. In that case, the gain becomes:

$$Gain_{DCvoltage} = -\frac{R_f}{R_{in}} \tag{2.5}$$

$$Gain_{ACvoltage} = -\frac{R_f}{R_{in}} \times \frac{1}{1 + 2\pi f C R_f} \tag{2.6}$$

2.2. Simulations and Construction

2.2.1. Electronic Circuit

One of the critical components is the operational amplifier. The signal is small and we need high gain. However, when the gain is high, the noise is also amplified and the output becomes noisy. The way to reduce this noise is to use a low-noise amplifier. LT1037 was chosen as a low noise and high speed opamp.

The simulations were performed with LtSpice which is used to simulate electronic circuits with high performance. It is a free SPICE (Simulation Program with Integrated Circuit Emphasis) based simulation program with an easy to use graphical user interface.

LtSpice schematics of the electronic circuit is shown in Figure 2.3. Based on our choice of r_f, r_{in} and C, the expected amplification is between 20-40 and response time less than 1 $msec$.

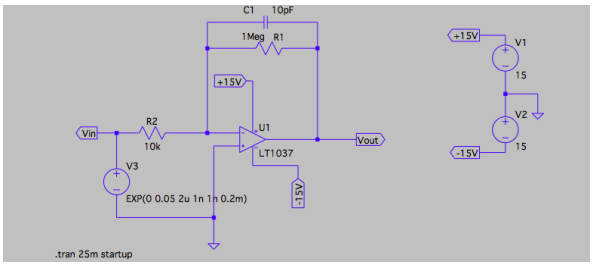

Figure 2.3. LtSpice Simulation scheme

The simulation has been done with a exponential pulsed signal which has a 50 mV amplitude 1 $nsec$ rise and 0.2 $msec$ fall edge. LT1037 has an operating voltage as 15 V.

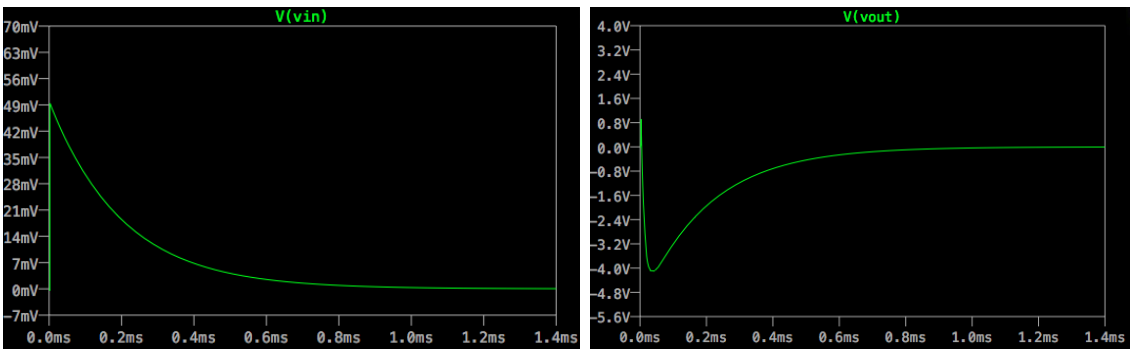

Figure 2.4. LtSpice Simulation results. Left: input pulse. Right: output signal.

The amplification result can be seen in Figure2.4. The amplification appearsto be around 80 times in this signal shape and frequency according to the simulations, however the simulations can be counted as the ideal case and the experimental result of the gain is expected to be than the simulation results.

2.3. Coil and Electronic Circuit Tests

The electronic circuit was constructed and installed into a metal box for shielding. The whole system was tested with a pulse generator before inserting it into the beam

line. Test setup can be seen in Figure 2.5.

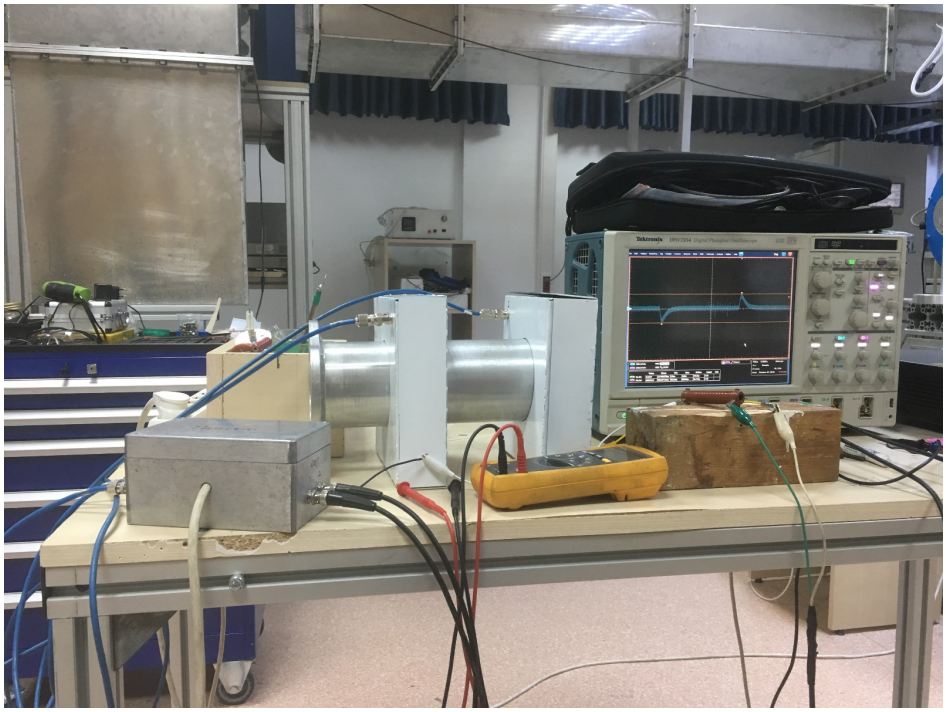

Figure 2.5. Test setup in SPP laboratory. Tne ACCTs are inside the white boxes in the middle of the setup.

Unlike the energy measurements, the current measurement only needs calibration data for ACCT which can be done with predefined pulses which have the same characteristics as the beam. Figure 2.6 shows the collected calibration data. The y axis of the plot is the voltage that was taken from ACCT and the x axis is the current of the pulse beam which is similar to the signal in the Section 2.2.1. Linear behavior shows us that the amplifying circuit is working as expected. The data have first been fit to a line and the intercept is observed to be consistent with zero. Concluding that there is no constant pedestal, we repeat the fit fixing the intercept to zero and obtain a calibration slope of $9.96 \pm 0.05 mV/\mu A$.

2.4. Experiment Setup And Results

SANAEM Project Prometeus(SPP) contains an educational proton beam line, which has a part called low energy beam transport(LEBT). LEBT line in SPP has two

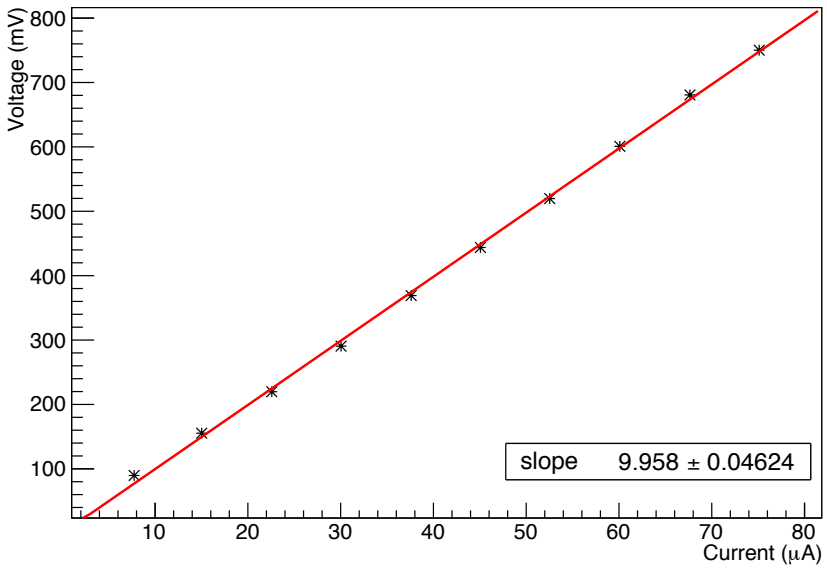

Figure 2.6. Calibration data with a linear fit.

diagnostic boxes and two ACCTs for measuring the beam characteristics. The first box has a pepper-pot plate for measuring the beam emittance and the second box has a Faraday cup for measuring the current of the beam. ACCTs were placed between the magnets so that the first diagnostic box remained between them [5].

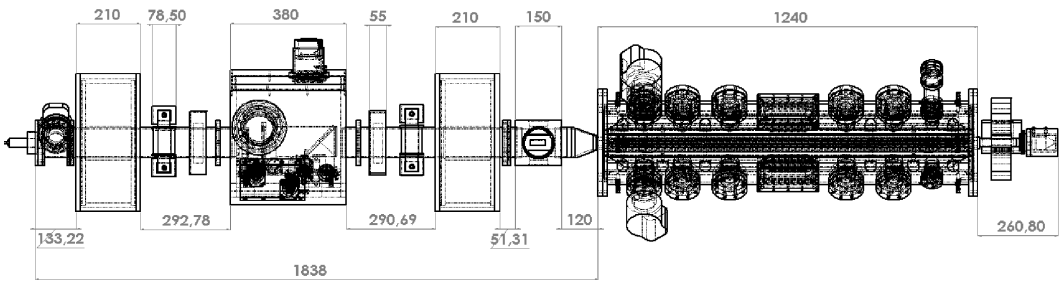

Figure 2.7. Sketch of the beam line

ACCT and Faraday cup results can be seen in Figure 2.8. The beam current that was measured using the Faraday cup is 12.5 μA. The current that was determined with the ACCT was obtained using the calibration from Figure 2.6 as $124.5mV/(9.96 \pm 0.05mV/\mu A) = 12.5 \pm 0.1\mu A$. Given the excellent agreement with the Faraday cup results, it can be undoubtedly said that the ACCT is working adequately for beam

current measurements.

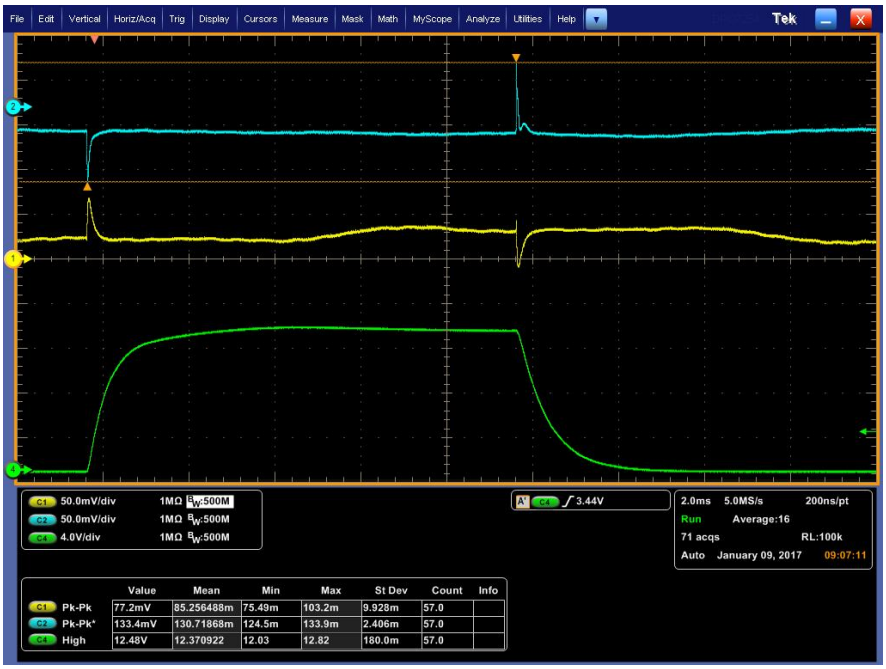

Figure 2.8. Beam current measurements. Green: Faraday cup, yellow and blue: ACCT signals. [5]

3. DWC: BEAM PROFILE AND EMITTANCE MEASUREMENTS

.

3.1. Historical Development of Gaseous Detectors

The exploitation of ionizing radiation started in 1895 with Wilhelm Röntgen who performed many experiments including taking the first photo of his wife's hand's skeletal structure with the X-Rays. This discovery was followed in 1896 by Henri Becquerel's observation that uranium salts giving off similar rays. Later, these rays were named by Marie Curie as radioactivity who was awarded Nobel Prize twice about radiation. Ernest Rutherford and Paul Villard classified radiation into three categories depending on their influence on the objects and their movement in the magnetic field: alpha, beta, and gamma. In the mean time, theory of the ionization mechanism was formulated by John Sealy Townsend between 1897 and 1901. With the theoretical development in ionization radiation, research on gaseous ionization detectors commenced with Hans Geiger under the supervision of Ernest Rutherford, culminating in the development of a device in 1908 which was later called the "Geiger Counter". However this counter could only detect alpha particles. In 1928, Geiger and Walther Müller improved the counter for detecting any kind of ionizing radiation (Figure 3.1).

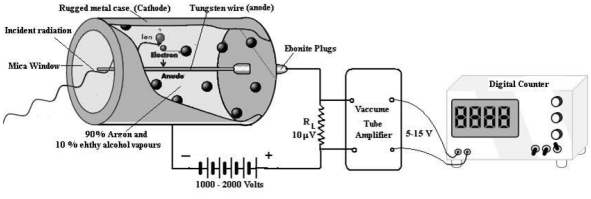

Figure 3.1. Schematics of the Geiger-Müller tubes [2]

Spark chamber, steamer chamber, bubble chamber and cloud chamber are amongst the early gaseous detectors. Gaseous detectors are generally used for tracking charged particles. The curvature of the trajectory of the particle under the magnetic field

gives us information about their momenta, and is related to the energy loss and mass of particles. Many of the elementary particles such as positron, muon etc have been found by these early detectors. The greatest revolution about gaseous detectors was in 1968 when Georges Charpak invented the Multi Wire Proportional Chamber (MWPC) which earned him the Nobel Prize in 1992. The multi wire proportional chamber can record up to one million tracks per second and its electronic readout allows interfacing directly to the computers. Multi wire chambers, and its follow-ups like drift chambers and time projection chambers have become valuable and crucial in high energy physics because of their speed and the precision. Over new readout techniques heve been searched for improving the spatial resolution of the MWPC. At the end using a delay line between the cathode wires was chosen for simplifying the data acquisition. That new device was called Delay Wire Chamber, which provides good resolution($\sim 200\ \mu m$) at low cost.

3.2. Theory

The theory of the gaseous particle detector depends on the interaction of charged particles with matter, drift and diffusion and Townsend avalanche. The brief explanation of the theoretical concepts will be given in this section.

3.2.1. Interaction of Charged Particles with Matter

There are many different energy loss mechanisms in the interaction of charged particles with matter such as Cherenkov radiation, bremsstrahlung, ionization, etc. depending on the particle's energy. The energy transfer arises from the probability of inelastic collisions which create excitation and ionization. Due to this inelastic process molecules can get ionized with the emission of photons or the appearance of free electron–ion pairs. The probability of the collision decreases with increasing energy transfer. The first incoming particles may interact with the medium, and the secondary particles that are created as a result of this interaction may also interact with the medium. In general, the last signal received in ionization detectors is influenced by the signals generated by the interactions of these secondary particles.

Table 3.1. Physical constants for various gases at NTP and approximate values of energy loss and ion-pair production (unit charge minimum ionizing particles). [6]

Gas	**Density**	$\mathbf{E_x}$	$\mathbf{E_I}$	$\mathbf{W_I}$	$\mathbf{\frac{dE}{dx}\ |_{min}}$	$\mathbf{N_p}$	$\mathbf{N_T}$
	$\mathbf{mgcm^{-3}}$	**eV**	**eV**	**eV**	$\mathbf{keVcm^{-1}}$	$\boldsymbol{cm^{-1}}$	$\mathbf{cm^{-1}}$
Ne	0.839	16.7	21.6	30	1.45	13	50
Ar	1.66	11.6	15.7	25	2.53	25	106
Xe	5.495	8.4	12.1	22	6.87	41	312
CH_4	0.667	8.8	12.6	30	1.61	37	54
C_2H_6	1.26	8.2	11.5	26	2.92	48	112
iC_4H_{10}	2.49	6.5	10.6	26	5.67	90	220
CO_2	1.84	7.0	13.8	34	3.35	35	100
CF_4	3.78	10.0	16.0	34	6.38	63	120

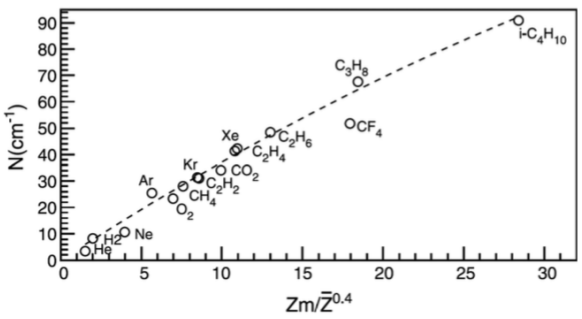

Figure 3.2. Primary ionization collisions per cm as a function of atomic number of gases at NTP [6].

Here we will describe a theoretical model for the ionizations following reference [6]. Assuming that the loss of energy by the incoming particle is small, the number of ionizations depends on a Poisson statistics; where n and k are the average and the actual numbers of pairs:

$$P_k^n = \frac{n^k}{k!} e^{-n} \tag{3.1}$$

The theoretical detector efficiency is then:

$$\varepsilon = 1 - P_0^n = 1 - e^{-n} \tag{3.2}$$

The total number of ion pairs were created inside a medium wthout recombination or any other side processes is:

$$N_T = \frac{\Delta E}{W_I} \tag{3.3}$$

where W_I is the average energy per ion pair.

From the Rutherford expression, for charge particle with velocity β_{rel}, the probability with releasing an energy between ϵ and $\epsilon + d\epsilon$ with a material thickness dx and density ρ can be written as:

$$\frac{d^2N}{dxd\epsilon} = K\frac{Z}{A}\frac{\rho}{\beta^2}\frac{1}{\epsilon^2} \tag{3.4}$$

An from the equation 3.4, K becomes:

$$K = \frac{4\pi N e^2}{mc^2} \tag{3.5}$$

e and m are the charge and mass of the electron, Z, A and ρ the medium atomic number, mass and density, and N Avogadro's number; in the CGS system of units the rest mass of the electron $mc^2 = 0.511\ MeV$ and $K = 40.308\ MeVg^{-1}cm^2$.

The differential energy loss called Bethe–Bloch equation is written as:

$$\frac{\Delta E}{\Delta x} = -\rho\frac{2KZ}{A\beta_{rel}^2}\left[\ln\frac{2mc^2\beta^2}{I(1-\beta^2)} - \beta^2 - \frac{C}{Z} - \frac{\delta}{2}\right] \tag{3.6}$$

where $\frac{C}{Z}$ represents the inner shell corrections, and $\frac{\delta}{2}$ is the density effect correction .

This formula shows that the energy loss from the ionization process is proportional to the particle's mass and the square of its charge. On the other hand, energy loss changes with the velocity of particle because with a slow velocity, the particle should spend more time in the medium which means it will interact more.The relation can be seen in Figure 3.3.

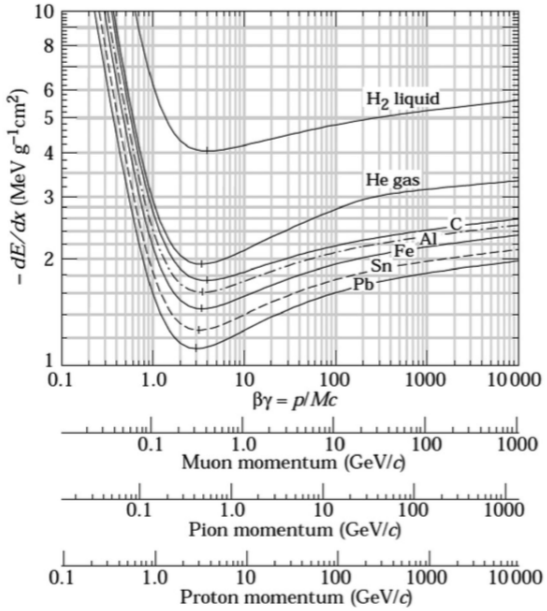

Figure 3.3. Differential energy loss as a function of velocity and momentum for singly charged particles in different materials. [6]

Voltage dependence vs. the number of ions created by the charged particles in the gas can be seen in Figure 3.4. Differential energy loss of the particles depend on particles' momentum and the material type.

3.2.2. Drift and Diffusion of Charged Particle in Gases

Ion and electron pairs in the ionized gas loose their energy because of collisions and converge on thermal energy distribution inside the gas. In the absence of an external field, they act like neutral particles and their behavior can be explained with the classic kinetic theory of gases [6]. The average value of the velocity is :

$$\bar{v} = \sqrt{\frac{8kT}{\pi m}} \tag{3.7}$$

and the mean free path of electron or ion:

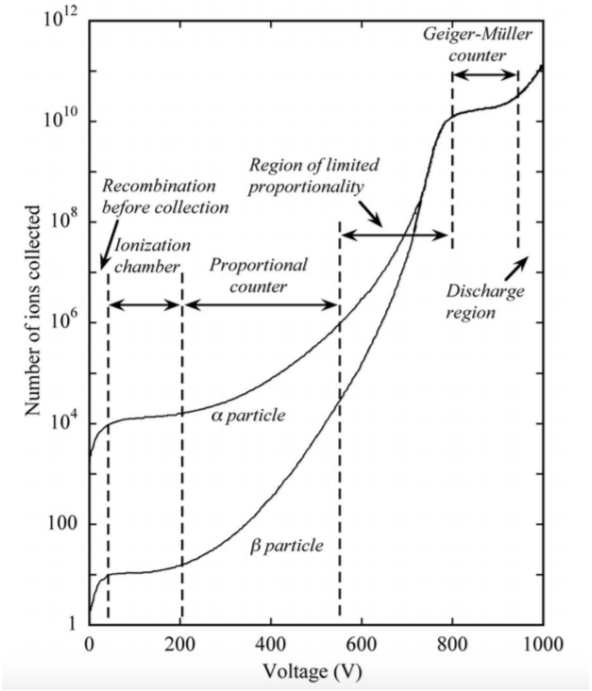

Figure 3.4. Voltage dependence of detected particle. [6]

$$\lambda = \frac{1}{\sqrt{2}} \frac{kT}{\sigma_{cs} P} \tag{3.8}$$

T is the temperature in Kelvin, k is the Boltzmann constant, P is the pressure and σ_{cs} is the effective cross-sectional area for collision.

Electrons and ions move along the field line under the influence of electric field. Mobility μ is :

$$\mu = \frac{w}{E} \tag{3.9}$$

w is the drift velocity and E is the electric field. Mobility of the particles is an important for the response time of the gaseous detectors.

3.2.3. Townsend Avalanche

Primary electrons that have been genarated from the ionization of the gas can also gain sufficient energy due to the high electric field and ionize the gas. Secondary electrons also create ionization and so on. This process is called avalanche multiplication.

Theoretical equations of the Townsend Avalanche are discussed in the reference [8]:

$$dn = n\alpha_2 dx \tag{3.10}$$

$$\mathbf{n} = n_0 \exp(\alpha_2 x) \tag{3.11}$$

$$M = n/n_0 = \exp(\alpha_2 x) \tag{3.12}$$

α_2 is the mean free path of the secondary electrons and $\frac{1}{\alpha_2}$ is the Townsend coefficient. n is the total number of created electrons, n_0 is the number of the electrons in the beginning and M is the multiplication factor. If the electric field is not uniform, α_2 becomes a function of x and the equation becomes:

$$M = \exp[\int \alpha_2(x)dx] \tag{3.13}$$

3.3. Multi Wire Proportional Chamber

Multi Wire Proportional Chamber(MWPC) is a gaseous detector which works in proportional region which can be seen in Figure 3.4 for tracking charged particles. MWPC is considered a revolutionary invention because of its speed and construction and utilization simplicity in experimental particle physics.

MWPC consists of equally separated anode wires between two conducting cathode planes which can be seen in Figure 3.5.

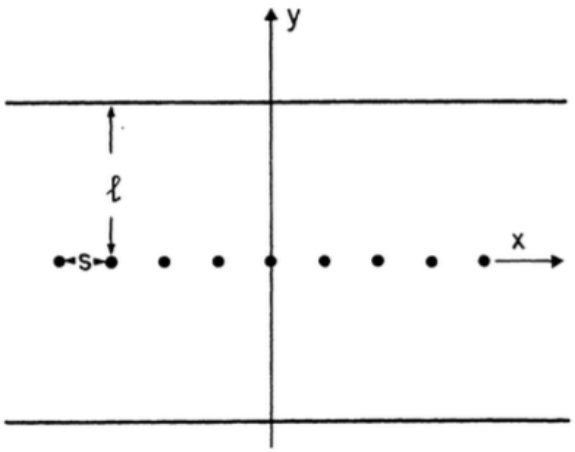

Figure 3.5. Construction schematics of MWPC. [7]

In that figure s represents the distance between anode wires and ℓ is the distance between anode and cathode planes.

Typical values of s is 2 to 5 mm while for ℓ is 5 to 10 mm. As can be seen in the figure the anode wires act like single proportional counters. The distance between anode wire is a crucial parameter for MWPC since it determines the spatial resolution of the chamber. The potential, electric field and capacitance relations of the detector are the following [7]:

$$V(x,y) = \frac{CV_0}{4\pi\epsilon_0}\left(\frac{2\pi\ell}{s} - \ln[4(\sin^2(\frac{\pi x}{s}) + \sinh^2(\frac{\pi y}{s}))]\right) \tag{3.14}$$

$$E(x,y) = \frac{CV_0}{2\pi\epsilon_0}\frac{\sqrt{1+\tan^2(\frac{\pi x}{s})\tanh^2(\frac{\pi y}{s})}}{\sqrt{\tan^2(\frac{\pi x}{s}) + \tanh^2(\frac{\pi y}{s})}} \tag{3.15}$$

$$C = \frac{2\pi\epsilon_0}{\frac{\pi\ell}{s} - \ln\frac{2\pi a}{s}} \tag{3.16}$$

a is the radius of the wires and V_0 is the applied voltage. The field lines can be seen in the Figure 3.6.

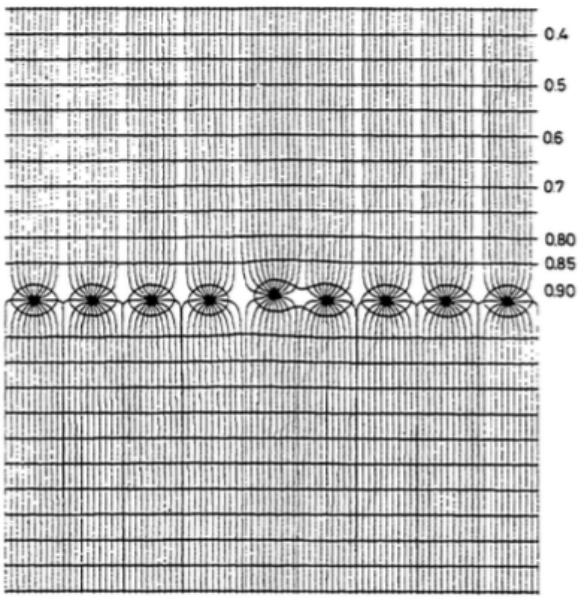

Figure 3.6. Equipotential voltage and electric field lines of MWPC. [7]

3.4. Delay Wire Chamber

3.4.1. Working Principle And Usage

Delay wire chamber is a gaseous detector which is a simplified version of MWPC. It was developed to improve the space resolution and as a side effect reduce the costs of the detector readout [9]. The main modification in the read-out system of DWC is to use a single readout circuit for all the wires. This is achieved by using a delay line between the cathode wires. This induces delays depending on which wire is closest to the incoming particle and by measuring the arrival time of the signals one can extract position. The DWC has a typical resolution of 200 microns.

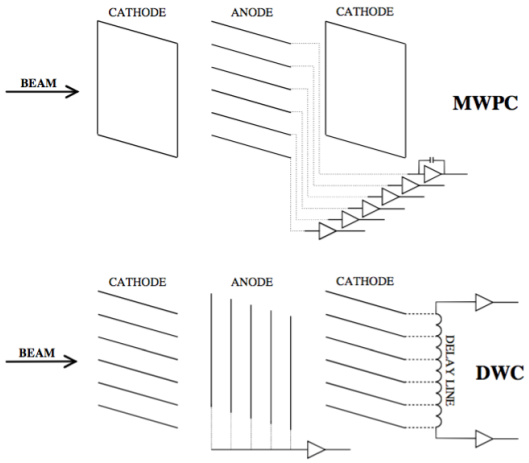

Figure 3.7. Standard MWPC read out against DWC read out. [9]

The working principle of Delay Wire Chamber is similar to Multi Wire Proportional chamber. The particle passes through the gas, ionizes it and creates electrons and positive ion pairs. When high voltages are applied to the anode wire, electrons drift towards to anode and the high electric field around the wires creates avalanche multiplication. These electrons create image charges in the cathode planes. Before the amplification, the generated electrical signals divided into two and passes trough the delay units. The position can be measured by obtaining the time difference between two parts of the signal (Figure 3.7).

3.4.2. Design And Simulations

The design of the chamber was performed with the open source program OpenSCAD [12]. This program is based on 3D modeling of the DWC layers with a basic script file. The design details can be found in the article [10]. Another script has been written for imploring the needs of an enduser which automatically produces the OpenSCAD input file that contains the design parameters, enabling endusers to easily design DWCs based on their particular needs.

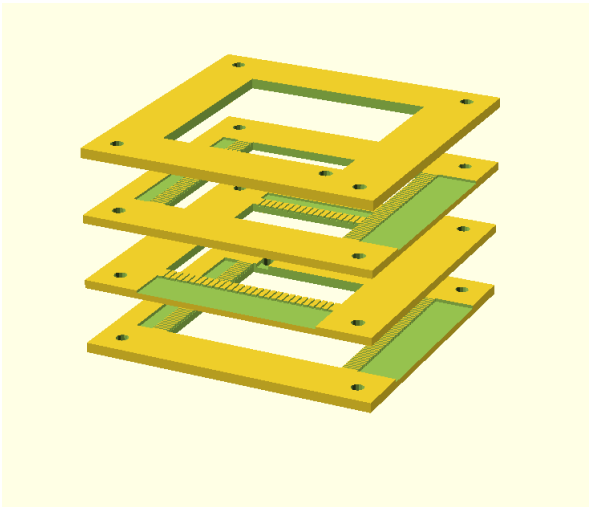

Figure 3.8. 3D design of cathode and anode layers.

The user input script requests necessary values of the chamber from the designer. With the answers taken from the user, it creates a text file which can be read by OpenSCAD and allows users to easily design a chamber with their parameters. The parameters requested from the user are the length of chamber, the length of a wire, the height of a layer, the height and width of the converter, the width of PCB, the radius of the screw hole on the the material chosen for the frame of the detector, position of hole, radius of wires, the gap between the cathode wires, the gap between the anode wires, font scale and height.

The electric field and particle tracking simulations have been performed with Garfield++. Garfield++ is an open source software which simulates the number of created electrons in the volume, the read-out signal which is generated by the electrons

and also simple electric field [13]. Garfield++ has integration with packages like Magboltz [14], which can calculate the characteristics of the gases in any kind of geometry. On the other hand, the main downside of this simulation program is the impossibility of adding cathode wires perpendicular to the anode wires. This problem has been solved by adding very thin cathode strips instead of wires for the electric field simulations.

The electric field simulations and tracking of a particle have been presented in a conference proceeding [11]. First, we have built the chamber geometry using our design parameters. Then the voltage was applied to the anode and the electric field simulations were performed (Figure 3.9).

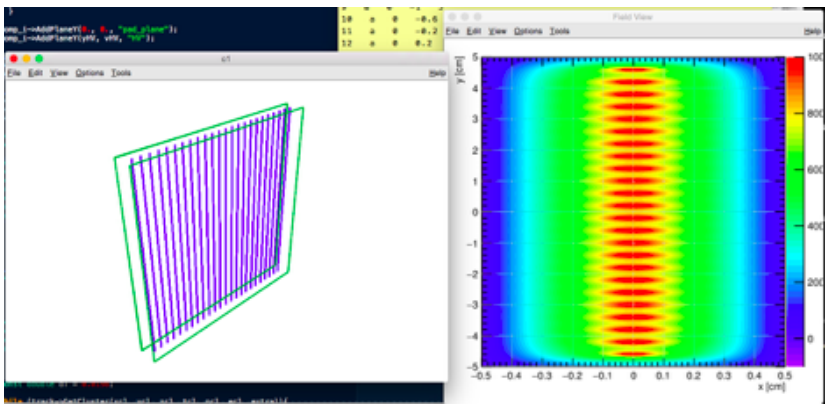

Figure 3.9. The electric field lines simulation of the chamber [11]

In the last stage, an electron gun was positioned $5mm$ away from the wires and the simulated signal can be seen in Figure 3.10.

3.4.3. Construction

The actual construction of the chamber started with preparing the frame of the chamber. Flame retardant 4 (FR4) material was chosen because of its high resistance to heat and electricity. Layers were cut by of a rotary saw and milling machine with respect to the plans in Figure 3.11. First, a large FR4 plate was divided into 19 $\times$19 cm small squares. The slots for placing readout circuit's PCB and PCB's for stretching the wires were opened with the milling machine. Converters were glued with epoxy due to epoxy's sturdiness and non-volatile feature.

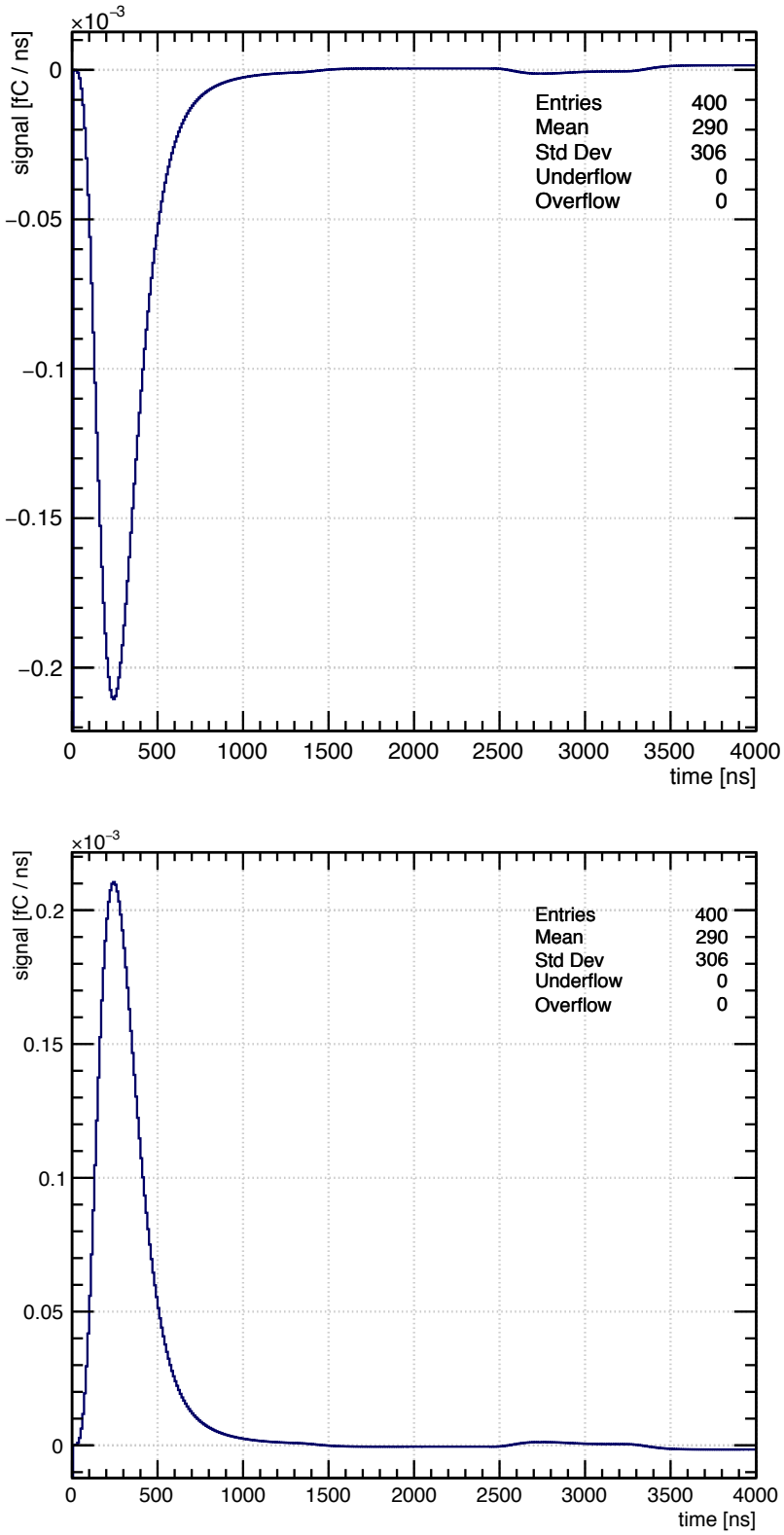

Figure 3.10. Anode and cathode signals generated by a particle that sent towards the chamber from an initial position 5 mmaway [11].

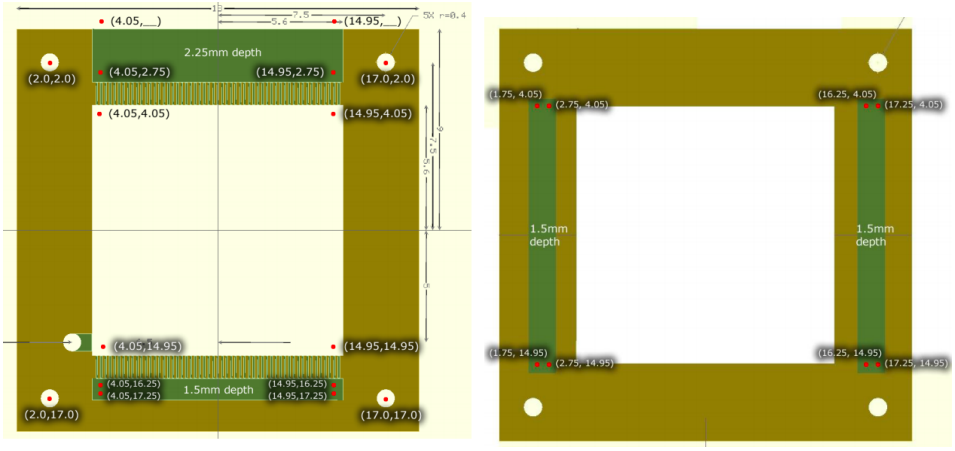

Figure 3.11. Schematics for cutting the FR4 frames.

The chamber for 2D position measurement has six layers, two of them are anode and the other four are cathode layers. Gold plated tungsten wire was used for anode wires, which have a 4 mm gap between them. Anode wires were positioned on a plane 4 mm away from cathode wires, which are copper-berrylium and has a 2 mm gap between them. Anode wires have a diameter of a 0.02 mm and cathode wires have diameter of 0.1 mm. The tensile strength of the copper-berrylium wire is 1000 N/mm^2 and the tensile strength of the gold plated tungsten wire is 1920 N/mm^2. By looking at the tensile strength, 100 gr and 20 gr sinkers were chosen to stretch the wires to the plate.

Figure 3.12. Stretching of the wires.

After stretching the wires, two procedures were applied to clean the chamber and wires after a suggestion by J. Spaangard in private communication. We baked to chamber for over 2 hours at a temperature of $150^0 C$. This is meant to protect the surface of the layer to any kind of damage that can come from sparking etc. The second procedure is an ultrasonic alcohol bath. All the layers were put into isopropyl alcohol bath inside the ultrasonic cleaner to clean the wires.

Figure 3.13. Baking in the owen and ultrasonic bath.

The first gas tests were done with a bubbler, although a humidity sensor was placed inside to box to be sure that good gas circulation was achieved. The measured relative humidity value started from 35% and got reduced down to 7.70% in three hours. This indicated to us that the gas circulation was achieved and our chamber was ready to trials.

3.4.4. Tests and First Results

Gas properties are important for gaseous ionization detectors. The avalanche multiplication quantity depends on the partial pressure of the gases and electric field strength at any given gas pressure. The gas mixture was chosen by considering this multiplication factor from Figure 3.15. 50%-50% CO_2-Ar mixture which is expected to yield approximately 50000 gas gain at 2.8 kV anode voltage [15], which was used for

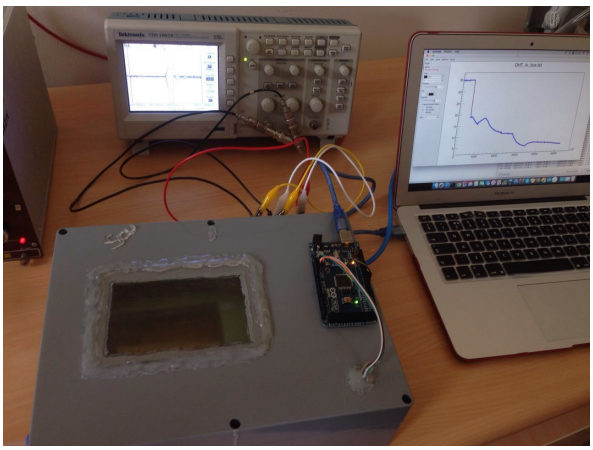

Figure 3.14. Humidity sensor setup

testing the chamber. Also primary ionization collision per cm for gases can be seen in Figure 3.2 and the energy loss of the particle can be calculated from equation 3.6 with using the constants in Table 3.1.

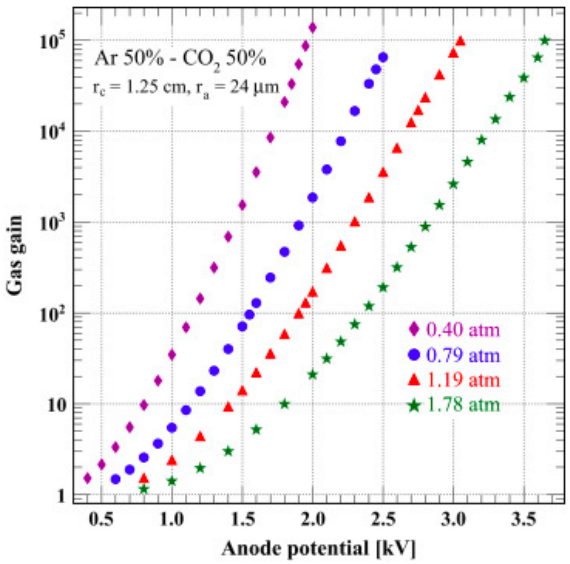

Figure 3.15. Gas gain due to Anode potential [15]

After the gas circulation was achieved, first tests were done with the basic circuit seen in Figure 3.16 implemented with a 27 $M\Omega$ resistor and 4.7nF ceramic capacitor.

The first observed signal can be seen in Figure 3.17. This signal was taken with collecting the signals from all wires.

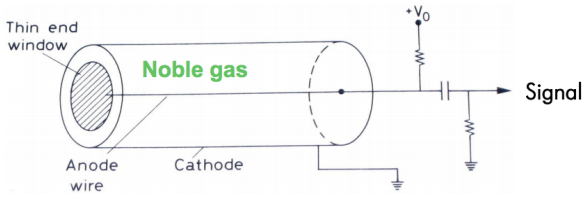

Figure 3.16. The basic readout circuit schema.

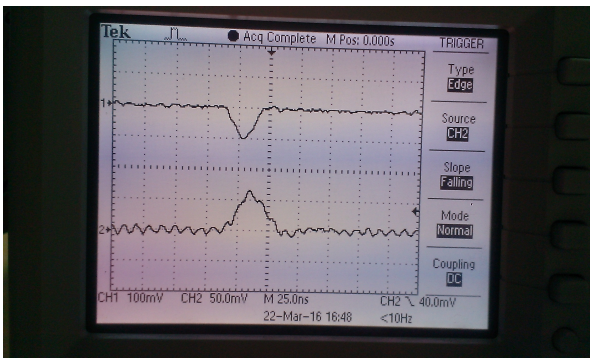

Figure 3.17. First signal

The read-out system of the DWC needs an electronic circuit, which we built in 3 different versions, starting with an original design from CERN. The first version of the electronic circuit was analyzed by one of my colleagues [16]. The study contains the electronic circuit design, simulation and implementation on hardware with a new approach. Unfortunately, stable results could not be achieved, however the study suggested the adding of a high-bandwidth buffer for stable operation.

In the second design of the readout PCB, we made changes to get stable results without a buffer by reserving one entire PCB layer only for grounding and another one for input voltages. Although the noise could be significantly reduced, we could not get the results that we expected. The circuit is very sensitive and has high gain thus, we add a tin shielding, which covers all the components in a Faraday cage(Figure 3.18).

The third version of the PCB was also soldered in our laboratory. The schematics of our design can be seen in Figure 3.19

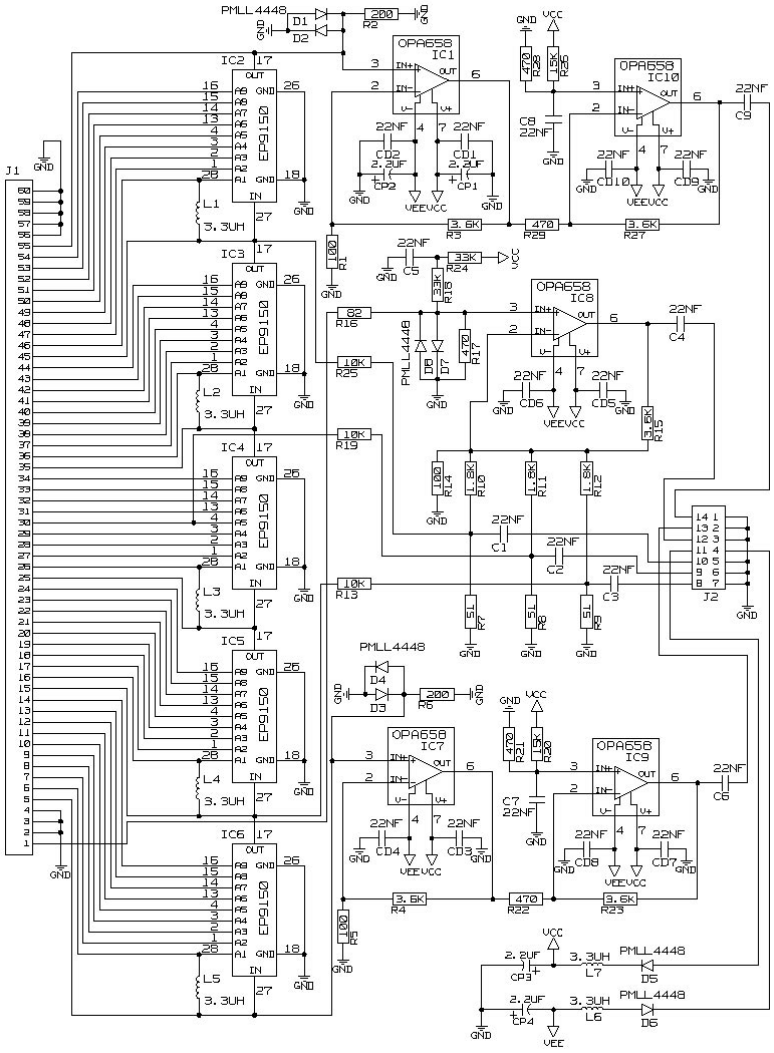

Figure 9. Local electronics diagram.

Figure 3.18. Original design of the read-out circuit [9]

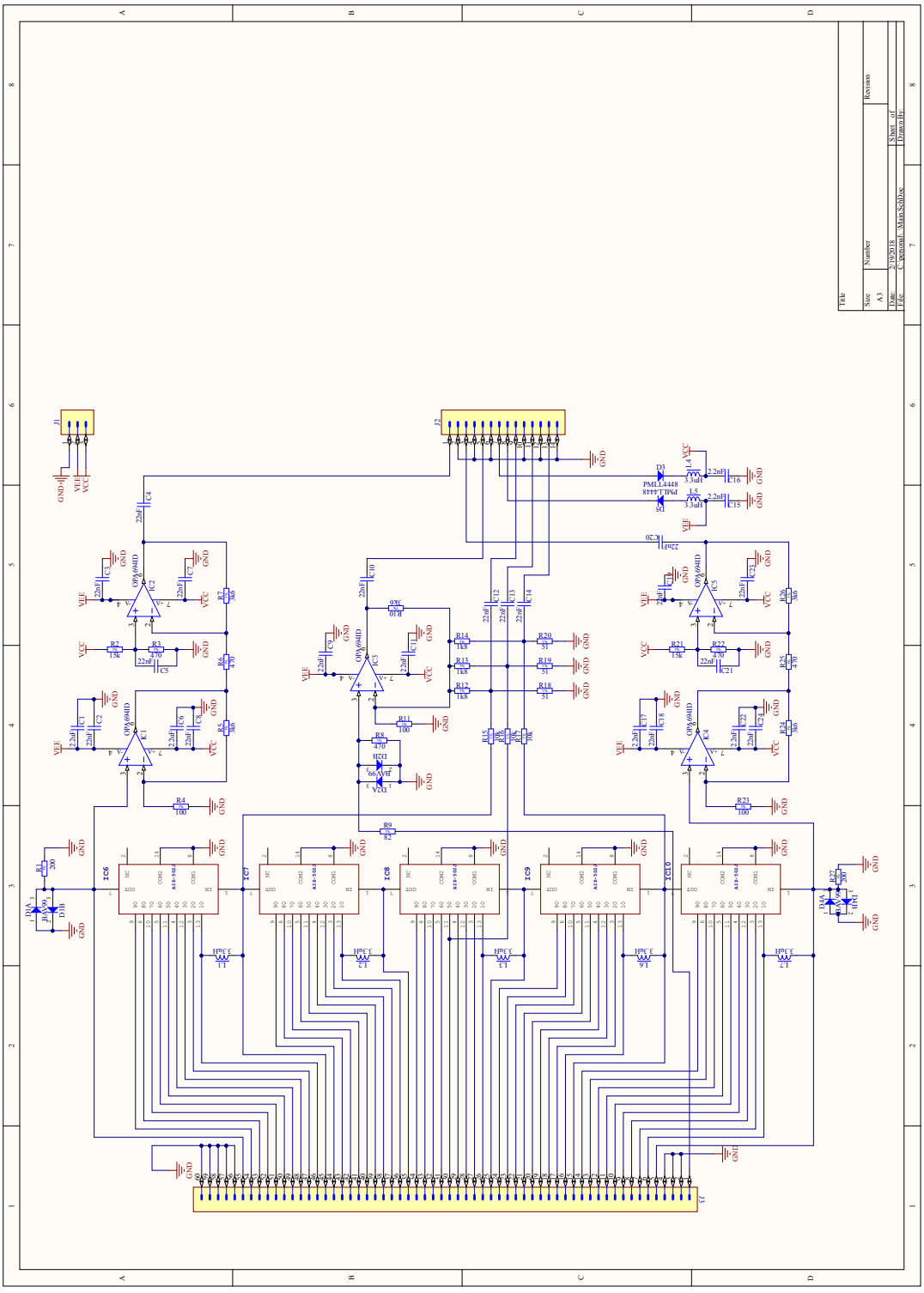

Figure 3.19. Our design of the circuit

The first tests of the third version were performed with a calibration pulse which has an amplitude of 40 mV over 50 Ω and a repetition rate of 10 kHz. The supply voltages of the circuit were set to ± 5 V.

In the Figure 3.20, the yellow test signal was taken from the pulse generator , blue and purple signals were the output of electronic circuit. The circuit amplifies the signal approximately 3 times.

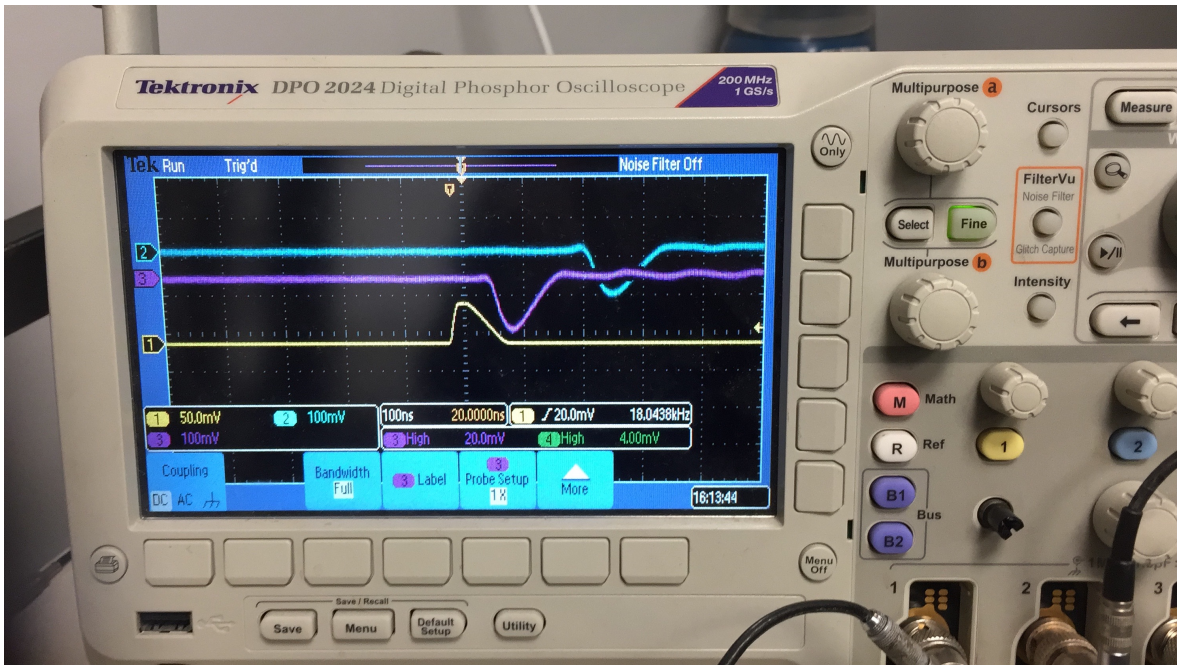

Figure 3.20. Test signal of the electronic circuit.Signals 2(blue)&3(purple) belong to the electronic circuit, 1(yellow) belongs to the generated pulse.

With the amplifier tests completed, test setup for the DWC was prepared. Test setup contains two PMT-scintillator layers and the DWC in between them. First, the working points of the PMT-scintillator setups were determined. For this purpose, initially the plateau voltages of the PMTs were obtained. Then counts and coincidence data were taken from the setup. Threshold of the detectors was 78 mV and data were taken for 200 sec. Two scintillators were parallel to each other and coincidence area was the largest. Applied voltage to PMT-1 and PMT-2 were 1.9 kV and 1.6 kV respectively. The results can be seen in Table 3.2.

Table 3.2. The individual and coincidence counts of the two sci-pmt setup

Trial	Sci-1	Sci-2	Coincidence
1	1984	3705	108
2	2026	3681	93
3	2052	3637	87
4	1953	3648	95
5	2009	3639	81

Since the coincidence counts had a relatively high variation, a second run was done with smaller coincidence area and bigger threshold (92 mV). The standard deviation(σ) and mean were calculated. The results can be seen in Table 3.3.

Table 3.3. The individual and coincidence counts of the two sci-pmt setup(second run)

Trials	Sci-1	Sci-2	Coincidence
1	1501	3198	47
2	1505	3152	38
3	1480	3030	37
4	1446	3070	38
5	1499	3008	43
mean	1486	3091	40.6
σ	24.4	80.9	4.27

DWC was then placed between the two pmt-scintillator setups for testing(Figure 3.21). Its high voltage was set to 2.8 kV. Two sci-pmt and DWC signals were connected to the oscilloscope and coincidence unit after discriminator. The threshold of the discriminator was 110 mV. Tests were done with cosmic particles.

Signals 1(yellow) and 2(blue) belong to the DWC, 4(green) belongs to the coincidence unit and 3(purple) belongs to the Sci-1.

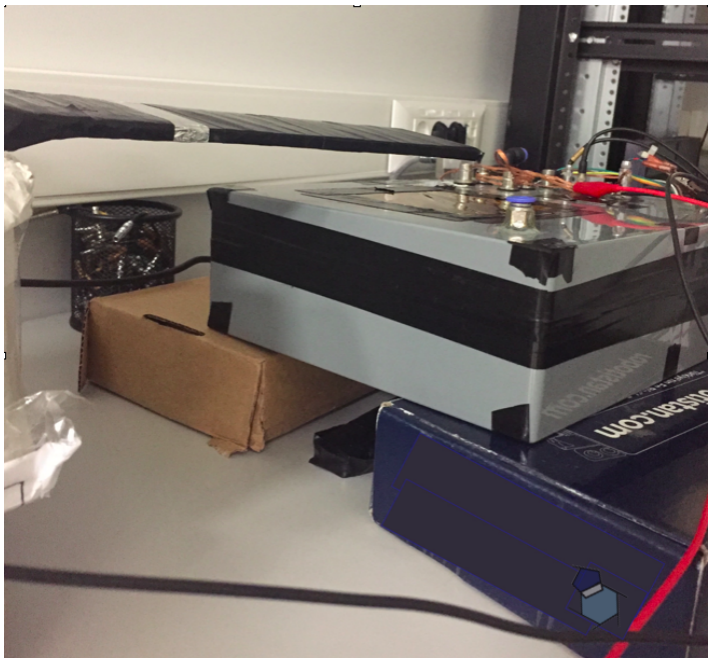

Figure 3.21. Sci-1(top) and Sci-2(bottom), DWC in between them.

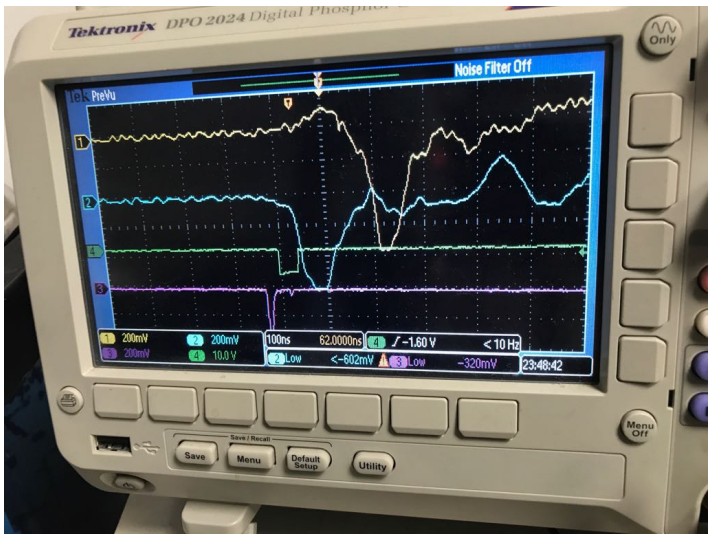

Figure 3.22. The signals and coincidence of the detectors.Signals 1(yellow) and 2(blue) belong to the DWC, 4(green) belongs to the coincidence unit and 3(purple) belongs to the Sci-1.

The coincidence signal from all three detectors were successfully observed from the test setup. One example is shown in Figure 3.22. However the rate of the coincidence was smaller than expected. A possible explanation would be that the threshold was too high to eliminate noise that came from the electronic circuit, so some of signals were missed.

4. TRANSPORT SOFTWARE: SIMULATING THE BEAM

4.1. General Theoretical Information

Beam diagnostics is a crucial concept in both accelerator and experimental particle physics. It covers the measurements of the beam profile, beam current, beam energy, emittance and Twiss parameters. These concepts will be briefly introduced in this section, before we describe the transport software written to simulate them.

4.1.1. Electromagnetic and Kinetic Relations

Electric and magnetic fields effect the trajectory and energy of charged particles through the Lorentz Force :

$$\overrightarrow{F} = \left(q\overrightarrow{E} + q(\overrightarrow{v} \times \overrightarrow{B}) \right), \tag{4.1}$$

where q is the charge of the particle and $\overrightarrow{v}$ is its velocity. Electric field can be used for both acceleration and deflection, whereas the magnetic fields can only be used for deflection. Especially in the high energy machines, magnetic fields are the only means of deflecting the beam. For circular machines, the centripetal force will be equal to Lorentz force and this leads us to define a quantity called "beam rigidity":

$$\begin{aligned} F = (qvB) &= \tfrac{\gamma m_0 v^2}{\rho}, \\ \gamma m_0 \overrightarrow{v} &= \overrightarrow{P}, \\ B\rho &= \tfrac{P}{q}. \end{aligned} \tag{4.2}$$

this can be used the normalization for the magnet strength.

In high energy cases dipole magnet normalized bending strength is defined as:

$$\frac{1}{\rho} = \frac{qB}{P}. \tag{4.3}$$

$\frac{1}{\rho}$ is in m^{-1}, the magnetic field B in T and and momentum P is in $\frac{GeV}{c}$.

For quadrupole magnets we can define, gradiant which gives the change in magnetic field with position:

$$g = \frac{\partial B}{\partial r}, \tag{4.4}$$

which leads us to normalized focusing strength of quadrupole:

$$k = \frac{g}{\frac{P}{q}} = \frac{g}{B\rho}. \tag{4.5}$$

4.1.2. Hamiltonian Mechanics and Phase Space

Many particle systems like beams are generally defined through Hamiltonian mechanics, which uses canonical coordinates position and momenta. 6-dimensional phase-space vector can be used for beam representations$(x, x', y, y', z, \delta)$. Particles can not follow the reference orbit; only the ideal particle (we call it the reference particle) follows the reference path.

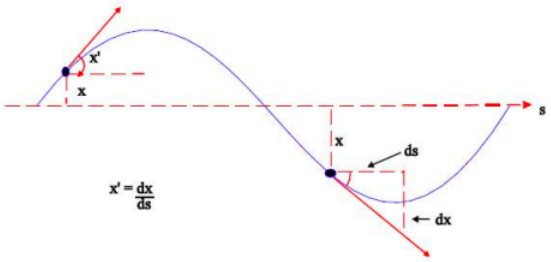

Figure 4.1. Transverse angles and phase space representation [18]

Defining s as the reference trajectory:

$$\begin{aligned} x' &= \frac{dx}{ds} \\ &= \frac{dx}{dt}\frac{dt}{ds} \\ &= \frac{v_x}{v_z} = \frac{P_x}{P_z} \\ &\approx \frac{P_x}{P_0}. \end{aligned} \tag{4.6}$$

where P_0 is the momentum of the reference particle ($P = P_0(1+\delta)$) and $\delta = \frac{\Delta P}{P_0}$. The same procedure can be done for y and y' and x' become the transverse momentum of the particles.

The transverse equation of motion can be expressed using the Hill Equations, which are homogenous differential equations for periodic motions:

$$x''(s) + K(s)x(s) = 0, \tag{4.7}$$

$$y''(s) + K(s)y(s) = 0. \tag{4.8}$$

where $K(s)$ represent the effect on the beam such as drift, quadrupole, solenoid etc.

General solution of the Hill's equations for the x direction and the corresponding x' are:

$$x(s) = \sqrt{\varepsilon}\sqrt{\beta(s)}\cos(\mu(s) + \mu_0), \tag{4.9}$$

$$x'(s) = -\frac{\sqrt{\varepsilon}}{\sqrt{\beta(s)}}(\alpha(s)\cos(\mu(s) + \mu_0) + \sin(\mu(s) + \mu_0)). \tag{4.10}$$

where ε, α, β and γ are unknowns of the general solution and from Equation 4.9 the unknowns become:

$$\begin{aligned} \cos(\mu(s) + \mu_0) &= \tfrac{x(s)}{\sqrt{\varepsilon}\sqrt{\beta(s)}}, \\ \alpha(s) &= -\tfrac{1}{2}\beta'(s), \\ \gamma(s) &= \tfrac{1+\alpha(s)^2}{\beta(s)}. \end{aligned} \tag{4.11}$$

If we take Equation 4.9 and Equation 4.10 together and solve for ε:

$$\varepsilon = \gamma(s)x(s)^2 + 2\alpha(s)x(s)x'(s) + \beta(s)x'(s)^2, \tag{4.12}$$

which is an elliptic representation of the phase space. ε is called the Courant-Synder invariant or geometric emittance, which stays constant throughout the motion. α, β and γ are named as the Twiss parameters which give the shape and orientation of the ellipse. ε is expressed in unit of $\pi.mm.mrad$ unit. According to Liouville theorem, the area of the phase space ellipse should be conserved if there is no change in the beam energy.

The geometric emittance is constant if only there is no acceleration, however we can define another important quantity called normalized emittance which is constant in motion even when there is acceleration:

$$\varepsilon_N = \beta_{rel}\gamma_{rel}\varepsilon_{geometric} \tag{4.13}$$

here $\beta_{rel} = \frac{v}{c}$ and $\gamma_{rel} = \frac{1}{\sqrt{1-\beta_{rel}^2}}$ are relativistic parameters.

4.1.3. Optics and Transfer Matrices

The focusing and defocusing effects of the quadrupoles can be thought as lenses. Each element has its own transfer matrix, which comes from the equation of motion of the particles. The equation of motion in x direction for particles along the beam path can be seen in Equation 4.7. For example, the solution of the equation of motion for quadrupole in focusing case and the derivative become:

$$\begin{aligned} x &= a\cos(\sqrt{k}s + b), \\ x' &= -a\sqrt{k}\sin(\sqrt{k}s + b). \end{aligned} \tag{4.14}$$

where a and b are constant, k is quadrupole strength. For $s = 0$, the equations become $x_0 = a\cos(b)$ and $x_0' = -a\sqrt{k}\sin(b)$. With using trigonometric relations, the equations can then be expressed as:

$$\begin{aligned} x &= a\cos(\sqrt{k}s)x_0 + \tfrac{1}{\sqrt{k}}\sin(\sqrt{k}s)x_0', \\ x' &= -\sqrt{k}\sin(\sqrt{k}s)x_0 + a\cos(\sqrt{k}s)x_0'. \end{aligned} \tag{4.15}$$

These can be written in the matrix form :

$$X = TX_0 \tag{4.16}$$

where T is called the transfer matrix. By applying similar methods to other beamline elements, various transfer matrices can be found. The best commonly used ones are:

$$T_{drift} = \begin{bmatrix} 1 & L \\ 0 & 1 \end{bmatrix} \tag{4.17}$$

$$T_{focus} = \begin{bmatrix} \cos(\sqrt{k}l) & \frac{1}{\sqrt{k}}\sin(\sqrt{k}l) \\ \sqrt{k}\sin(\sqrt{k}l) & \cos(\sqrt{k}l) \end{bmatrix} \tag{4.18}$$

$$T_{defocus} = \begin{bmatrix} \cosh(\sqrt{k}l) & \frac{1}{\sqrt{k}}\sinh(\sqrt{k}l) \\ \sqrt{k}\sinh(\sqrt{k}l) & \cosh(\sqrt{k}l) \end{bmatrix} \tag{4.19}$$

$$T_{sol} = \begin{bmatrix} \cos^2(Kl_s) & \frac{1}{K}\cos(Kl_s)\sin(Kl_s) & \cos(Kl_s)\sin(Kl_s) & \frac{1}{K}\sin^2(Kl_s) \\ -K\cos(Kl_s)\sin(Kl_s) & \cos^2(Kl_s) & -K\sin^2(Kl_s) & \cos(Kl_s)\sin(Kl_s) \\ -\cos(Kl_s)\sin(Kl_s) & -\frac{1}{K}\sin^2(Kl_s) & \cos^2(Kl_s) & \frac{1}{K}\cos(Kl_s)\sin(Kl_s) \\ K\sin^2(Kl_s) & -\cos(Kl_s)\sin(Kl_s) & -K\cos(Kl_s)\sin(Kl_s) & \cos^2(Kl_s) \end{bmatrix} \tag{4.20}$$

In these matrices, L is the drift length, l is the quadrupole length, K is the solenoid strength and l_s is the solenoid length.

The beam motion can easily be modeled with such transfer matrices from an initial position r_1 to some final position r_2. The linear transformation of the beam matrix σ can be shown as:

$$\begin{aligned} \sigma_{ij}(1) &= T\sigma_{iij}(0)T^T. \\ \sigma_{11}(1) &= T_{11}^2\sigma_{11}(0) + 2T_{11}T\sigma_{12}(0) + T_{12}^2\sigma_{22}(0). \end{aligned} \tag{4.21}$$

And from the Equation 4.12, the elements of the σ matrix are :

$$\begin{aligned} \sigma_{11}(0) = x_{max}^2 &=< x^2 >= \beta\varepsilon, \\ \sigma_{12}(0) &=< xx' >= -\alpha\varepsilon, \\ \sigma_{22}(0) &=< x'^2 >= \gamma\varepsilon. \end{aligned} \tag{4.22}$$

where x_{max} is the beam width.

4.2. Beam Diagnostic Instruments and Methods

4.2.1. Emittance Measurement With Three Monitor Method

Three monitor method is a frequently used emittance measuring technique for low current beams that do not suffer much from space-charge effects. The measurement depends on measuring the beam width at three different position with three different detectors. The width is proportional to $\beta\varepsilon$ as can be seen in Equation 4.22. For finding the emittance, Equation 4.21 which has three unknowns, should be solved to determine

the $\sigma_{11}(0)$.

A computer code has been developed to calculate the beam emittance by taking the spot size of the beam in three different positions directly from the beam transport program. This code can also be used to calculate the beam emittance using the experimental results. The code can be seen in Appendix A. The results that are taken from the Beam Transport Program, which will described in the next section, also can be used to calculate the emittance with three monitor method which will help us to compare the experimental results with simulations.

4.3. Beam Transport Program

4.3.1. Purpose and General Information

A beam transport program has been written in C++ for modeling the evolution of the beam parameters, when the beam drifts a distance or goes through the quadrupole and solenoid magnets. In addition, the program also does calculations for two different emittance measurement methods with the given parameters. Moreover, the ROOT library is used to plot the results [17].

The program needs some input parameters to create beam such as rest mass of the particles, their kinetic energy, the initial normalized emittance, the beam width in both planes and the total number of particles inside the beam. The program automatically calculates Twiss parameters and geometric emittance and creates a beam with a bivariate Gaussian distributed particle density.

Drift space, quadrupole and solenoid magnets can be added to calculate beam parameters after these transport elements. The transport library of this program will also be used in the low energy beam transport section of Demirci, which is a computer program for RFQ design [19].

4.3.2. Beam simulations and results

The whole program code can be seen in Appendix A. The example proton beam was created with 10 MeV energy and with a normalized emittance of 0.01 $\pi.mm.mrad$ and with a beam width of 10 mm. The beam created using these parameters can be seen in Figure 4.2.

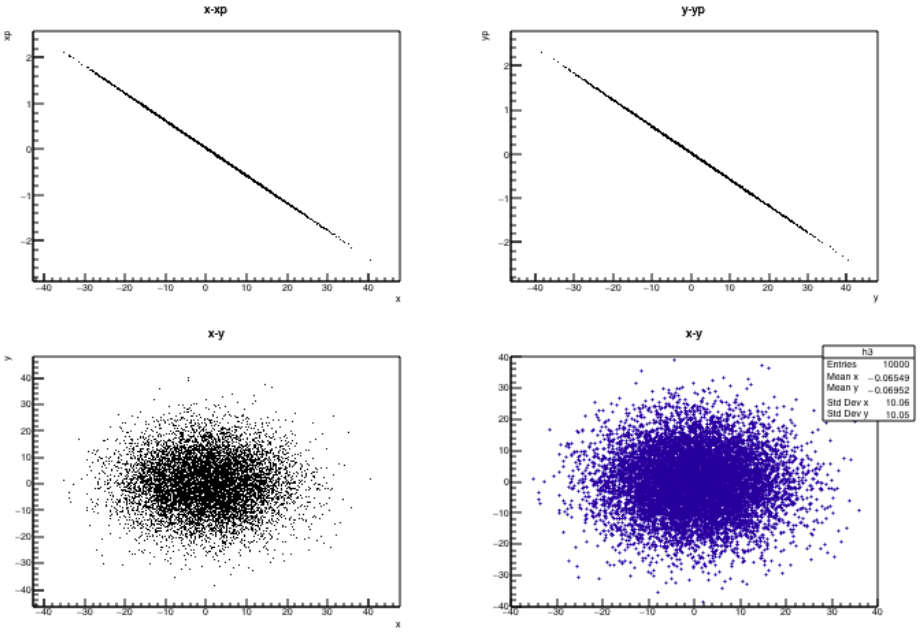

Figure 4.2. The initial beam created by the Beam Transport Program for 10 MeV proton beam with 0.01 normalized emittance and 10 mm beam width.

After the creation of the beam, it was made to drift $1m$ and the new beam parameters were calculated with the transfer matrix in Equation 4.17. The $x - x'$, $y - y'$ and $x - y$ distribution of the particles can be seen in Figure 4.4.

As a last stage the beam was put into quadrupole and solenoid magnets after drifting separately. The graphs of the particle distributions can be seen in Figure 4.6 and Figure 4.8.

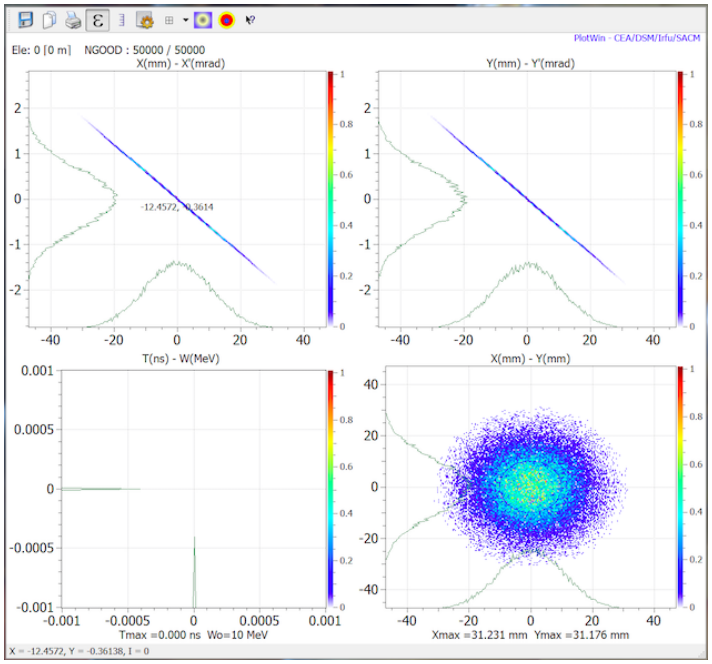

Figure 4.3. The initial beam created by the Travel program with the same input parameters as those used for Figure 4.2.

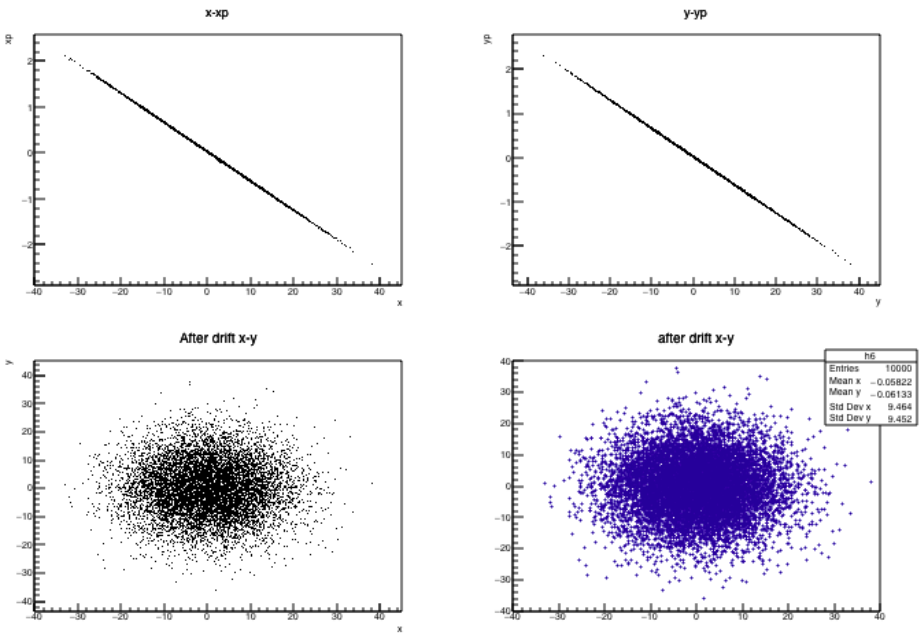

Figure 4.4. The $x - x'$,$y - y'$ and $x - y$ distribution of the particles after 1 m drift.

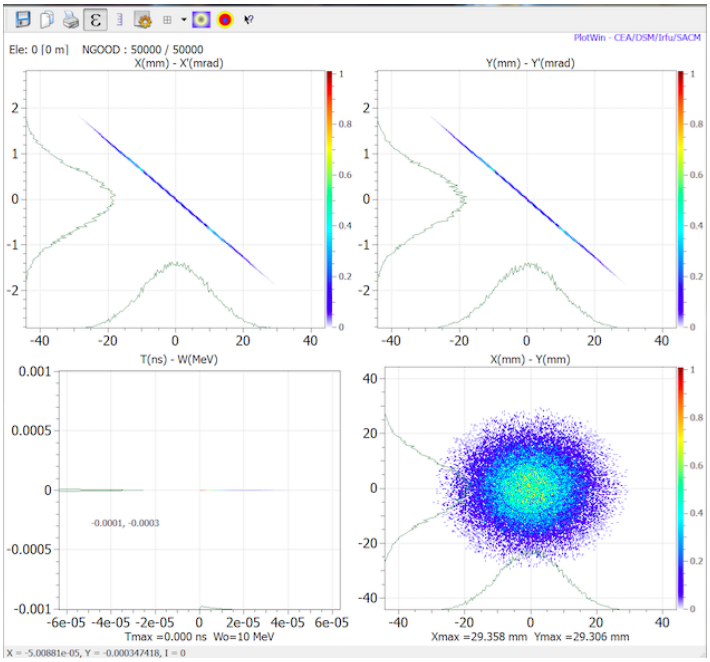

Figure 4.5. The $x - x'$,$y - y'$ and $x - y$ distribution of the particles after 1 m drift obtained with Travel.

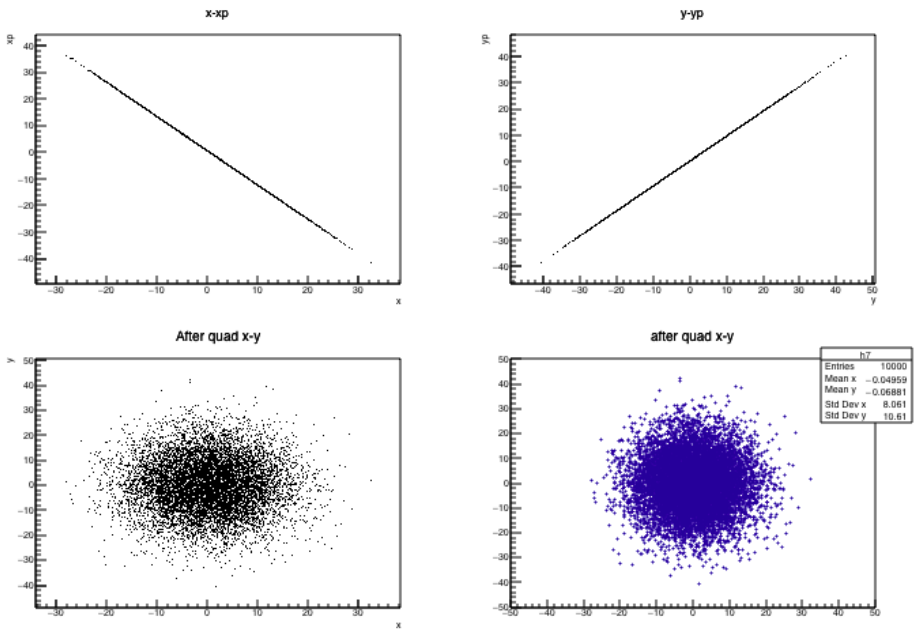

Figure 4.6. The $x - x'$,$y - y'$ and $x - y$ distribution of the particles after 1 m drift and quadrupole magnet.

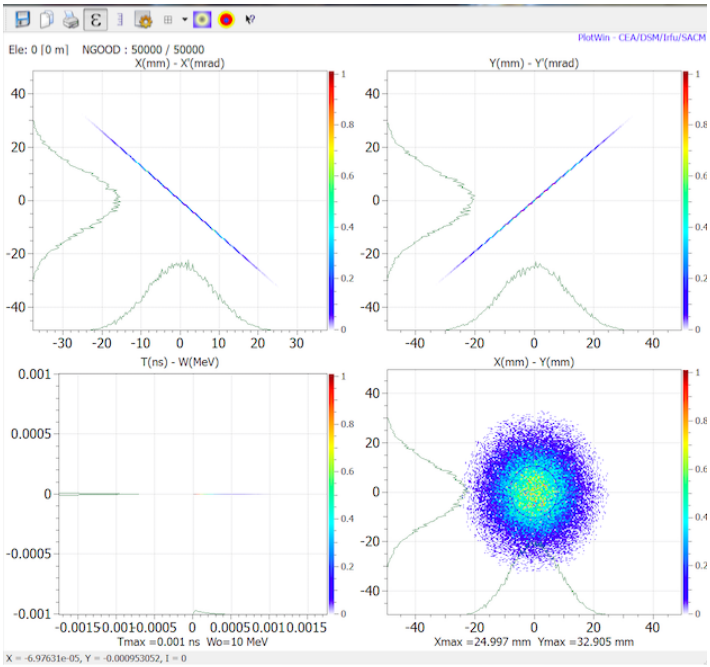

Figure 4.7. The $x - x'$,$y - y'$ and $x - y$ distribution of the particles after 1 m drift and quadrupole magnet obtained with Travel.

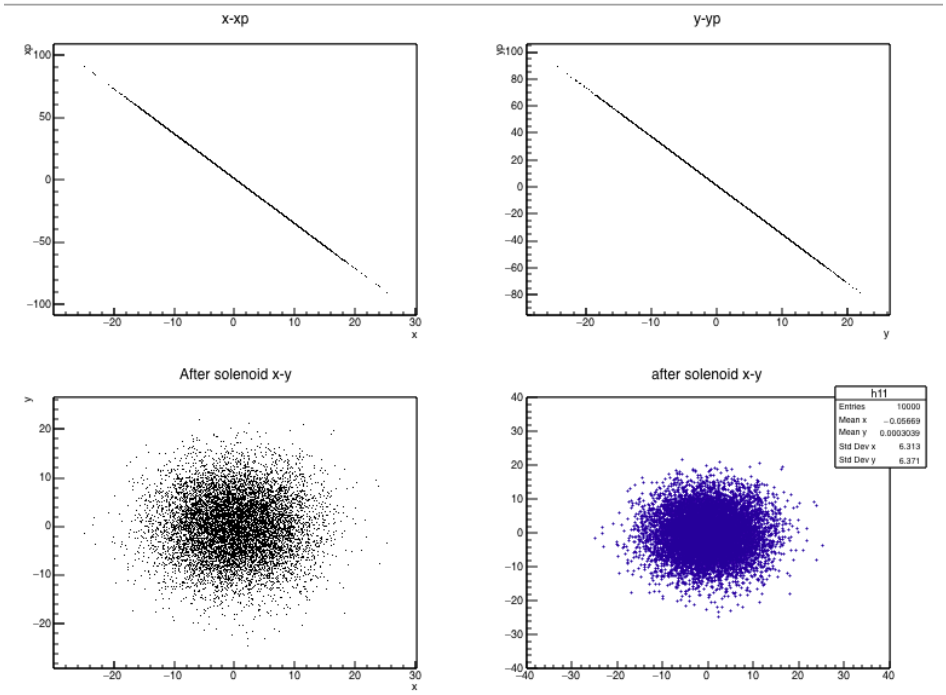

Figure 4.8. The $x - x'$,$y - y'$ and $x - y$ distribution of the particles after 1 m drift and solenoid magnet.

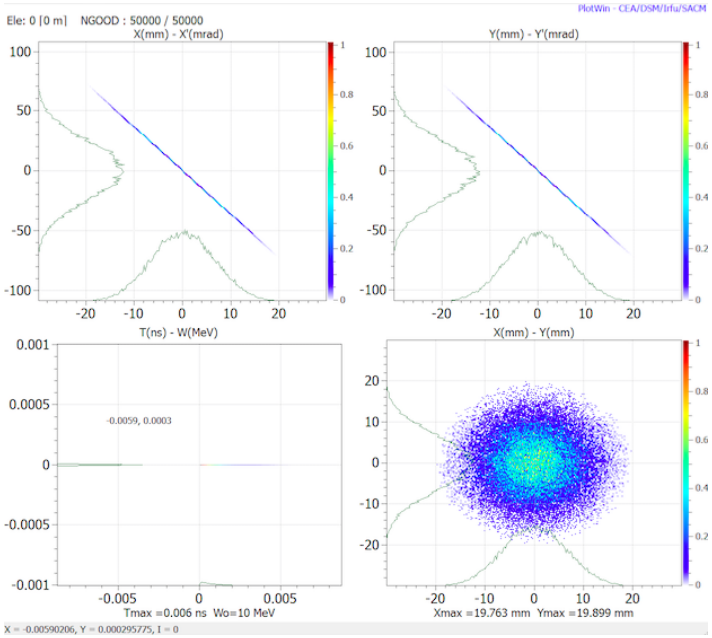

Figure 4.9. The $x - x'$,$y - y'$ and $x - y$ distribution of the particles after 1 m drift and solenoid magnet obtained with Travel.

4.3.3. Comparison of Beam Transport Program Results and Simulations

The comparison of the beam transport program was done against the software Travel. Travel is a particle-tracking program which was developed at CERN. The procedure described in the previous subsection was repeated with the Travel program and these results can be seen in Figures 4.3, 4.5, 4.7 and 4.9.

The graphical output of Travel and our Beam Transport program are comparable. The Beam Transport program also calculates Twiss parameters, geometric and normalized emittances after each beam element. All equations needed for calculations can be seen in Section 4.1. Table 4.1 contains the Twiss parameters and emittance results of the initial beams that were created by Beam Transport Program and Travel separately.

The evolution of the Twiss parameters via transfer matrix calculation has not been implemented for solenoid in the Beam Transport Program code yet, so the emittance and Twiss parameter calculations were done with an external C program, which

Table 4.1. $x - x'$ emittance and Twiss parameters from two different programs computed for the initial beam.

Parameter	Travel	Beam Transport P.
α Alpha(mrad)	87.8456	87.8454
β Beta(mm)	1464.0931	1464.09
γ Gamma(1/mm)		5.27141
β_{rel} Relativistic beta	0.144844	0.144865
γ_{rel} Relativistic gamma	1.010065	1.01066
ε Emittance(mm.mrad)	0.0683518	0.0692368
ε_{norm} Normalized emittance	0.0100	0.0101371

Table 4.2. $x - x'$ emittance and Twiss parameters from two different programs computed after 1 m drift.

Parameter	Travel	Beam Transport P.
α Alpha(mrad)	82.5741	82.574
β Beta(mm)	1293.6721	1293.67
γ Gamma(1/mm)		5.27141
β_{rel} Relativistic beta	0.144844	0.144865
γ_{rel} Relativistic gamma	1.010065	1.01066
ε Emittance(mm.mrad)	0,0683518	0.0692383
ε_{norm} Normalized emittance	0.0100	0.0101371

Table 4.3. $x - x'$ emittance and Twiss parameters from two different programs computed after 1 m drift and quadrupole magnet.

Parameter	Travel	Beam Transport P.
α Alpha(mrad)	1208.5738	1250
β Beta(mm)	937.6851	938.507
γ Gamma(1/mm)		1474.27
β_{rel} Relativistic beta	0.144844	0.144865
γ_{rel} Relativistic gamma	1.010065	1.01066
ε Emittance(mm.mrad)	0.0683518	0.0692387
ε_{norm} Normalized emittance	0.0100	0.0101372

was taken from Gökhan Ünel in private communication and it can be found in Appendix A.

Table 4.4. $x - x'$ emittance and Twiss parameters from two different programs computed after 1 m drift and solenoid magnet.

Parameter	Travel	Beam Transport P.
α Alpha(mrad)	2104.3069	2126.94
β Beta(mm)	578.8601	588.495
β_{rel} Relativistic beta	0.144844	0.144865
γ_{rel} Relativistic gamma	1.010065	1.01066
ε Emittance(mm.mrad)	0.0683518	0.0677175
ε_{norm} Normalized emittance	0.0100	0.00991302

The differences between the calculated values from Travel and Beam Transport Program are on the order of 1%. The methods in the Beam Transport Program have also been implemented into Demirci, however GNU Scientific Library was used instead of ROOT. The relevant section of DemirciPRO GUI where the beam transport is used can be seen in Figure 4.11 and 4.10.

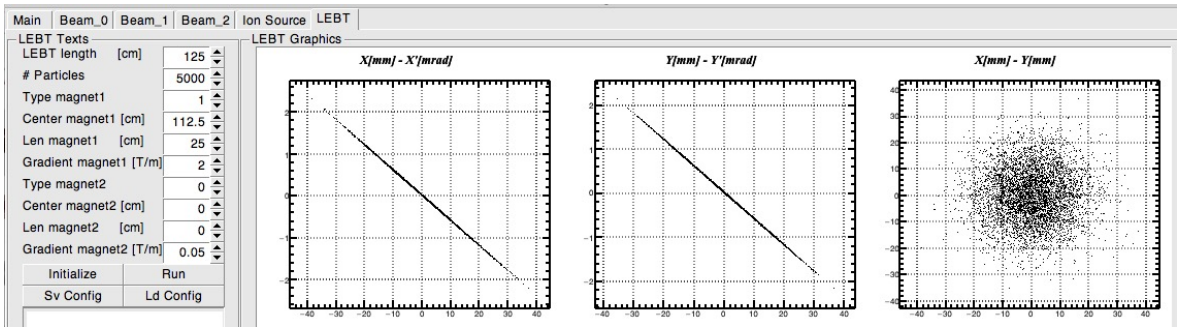

Figure 4.10. The $x - x'$,$y - y'$ and $x - y$ distribution of the initial particles.

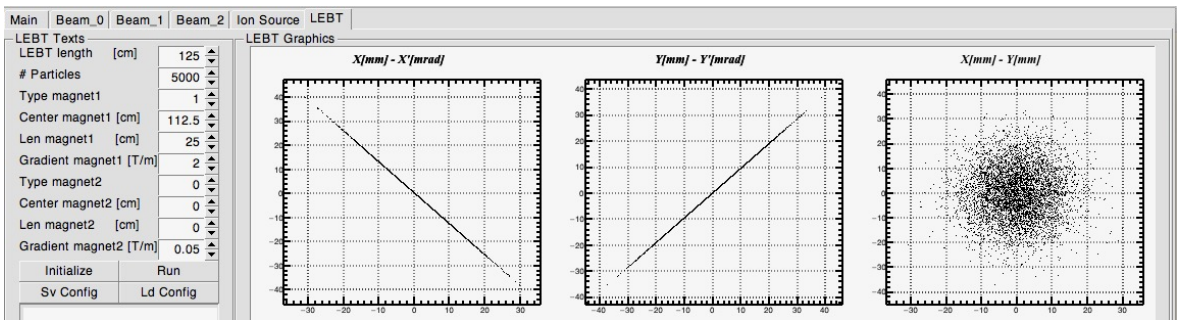

Figure 4.11. The $x - x'$,$y - y'$ and $x - y$ distribution of the particles after 1 m drift, quadrupole magnet.

5. CONCLUSION

In this thesis, the design and construction of a delay wire chamber and an AC current transformer were described and finally the constructed as well the tests of the constructed devices in preparation for beam measurements at actual accelerators. Also, a Beam Transport Program was written to simulate the beam evolution along the beam line.

ACCT's electronic circuit and mechanics were tested in the SPP beam line and compared with the results of the Faraday cup. The excellent agreement between the two results leads us to conclude that the ACCT design presented in this thesis can be used in future beam current measurements at the KAHVE Laboratory.

The DWC project was supported by TÜBİTAK under the grant id 114F467. While the constructed DWC's electronic circuit still has same noise issues, the chamber is considered ready test on a beamline.

The beam transport program results have been compared with the benchmark program Travel and the difference between the results is better than 1%. Beam transport program functions have also been incorporated into Demirci, the graphical RFQ design program developed in Turkey with support from TÜBİTAK under grant id 114F106.

In conclusion, for electron and proton accelerators that have been planned to be built at the KAHVE Laboratory, the beam measurement devices have been built and tested. The devices and transport program to be used in the future machines can be produced following the know how summarized in this thesis. Also, this thesis shows that commercial components are not needed to understand the beam. For example, a program which has been written an academic semester can do the same job properly.

REFERENCES

1. Analog Devices Company, *LTSpice*, http://www.linear.com/solutions/ltspice, accessed at May 2018.

2. A.Mourya, *Geiger Muller Counter*, https://sites.google.com/site/-puenggphysics/home/unit-iii/gm-counter, accessed at May 2018.

3. H.Wiedemann, *Particle Accelerator Physics*, *3rdedition*, Springer, Berlin, Heidelberg, NewYork, 2007.

4. Aspencore Network, *Electronic tutorials*, https://www.electronics-tutorials.ws/transformer/current-transformer.html, accessed at May 2018.

5. G. Turemen *et al.*, "Pulsed beam tests at the SANAEM RFQ beamline", *2017J.Phys.* : *Conf.Ser.874012045*.

6. F. Sauli, "Gaseous Radiation Detectors: Fundamentals and Applications", *CambridgeUniversityPress*, *Cambridge*, *2014*, *pp.iii − iii*.

7. F. Sauli, "Principles of Operation of Multiwire Proportional and Drift Chambers", *CERN77 − 09*, *1977*.

8. W.R. Leo, *Techniques for Nuclear and Particle Physics Experiments*, Springer, 1994.

9. J.Spanggaard, "Delay Wire Chambers A User's Guide.", *SL − Note − 98 − 023(BI)*, *CERN − SLDIVISION*, *Geneva*, *Switzerland*, March 1998.

10. S.Gurbuz *et al.*, "A wire chamber for educational purposes", *arXiv* : *1409.0523*[*physics.ins − det*], September 2014.

11. E.Ergenlik *et al.*, "Design, Simulation And Construction Of The Delay Wire Chamber", *AIP Conference Proceedings 1935, 070003(2018); doi : 10.1063/1.5025984*, 2018.

12. OpenSCAD, *The Programmers Solid 3D CAD Modeller*, http://www.openscad.org, accessed at April 2018.

13. Garfield, "A Drift-Chamber Simulation Program", *CERN Program Library entry W5050*, http://garfield. web.cern.ch, accessed at April 2018.

14. S. Biagi, *CERN program library*, http://magboltz.web.cern.ch/magboltz/, accessed at April 2018.

15. Ö.Şahin *et al.* "High-precision gas gain and energy transfer measurements in Ar – CO2 mixtures", *Nucl.Instr.Meth.Phys.Res.A, 768(2014), pp.104 − 111*, 2014.

16. Z.İstemihan, *Design, Simulation And Construction of A Wire Chamber Electronics*, 2017, M.Sc. Thesis, Boğaziçi University, Turkey, 78 p.

17. CERN, *ROOT* , https://root.cern.ch/, accessed at June 2018.

18. CERN, *Taking a Closer Look At LHC*, https://www.lhc-closer.es/taking_a_closer_look_at_lhc/0.complex_movement, accessed at July 2018.

19. B.Yasatekin, G.Turemen and G.Unel, "A Graphical Approach to Radio Frequency Quadrupole Design", *ComputerPhysicsCommunications, Volume192, 108 − 113*, 2015.

APPENDIX A: EMITTANCE CALCULATION AND BEAM TRANSPORT CODES

The three monitor method emittance calculation, beam transport and external emittance calculation codes can be found in CD which was given with this thesis.